

A PERFUSED TUMOR FLOW PHANTOM FOR IRON OXIDE MAGNETIC
NANOPARTICLE-MEDIATED HYPERTHERMIA STUDIES

By

JOLIN PHILENTHA RODRIGUES

A THESIS PRESENTED TO THE GRADUATE SCHOOL
OF THE UNIVERSITY OF FLORIDA IN PARTIAL FULFILLMENT
OF THE REQUIREMENTS FOR THE DEGREE OF
MASTER OF SCIENCE

UNIVERSITY OF FLORIDA

2013

© 2013 Jolin Philentha Rodrigues

To Mama, Papa, Joanne and Ausby

ACKNOWLEDGEMENTS

Having been blessed with remarkable parents who have been the bedrock of my life and the voice of encouragement in all my endeavours, words aren't enough to express my intense gratitude for them. I thank them for having more faith in me than I did in myself. I owe this thesis to you, as I reach another milestone you helped me achieve. My younger brother and sister, Joanne and Ausby, have never failed to provide me with kind words and unconditional love at every step in my life. I owe them my love and heartfelt thanks as well.

My sincere gratitude goes to my advisor, Dr. Jon Dobson, for giving me a chance to explore the field of nanobiomagnetism, to learn much from it, and grow as a scientist along the way. I also thank him for financially supporting me whenever possible, and being constantly encouraging of my thesis work. I specially thank my committee members Dr. Rinaldi, Dr. Batich and Dr. Allen for being on my committee and never failing to respond promptly whenever I needed some advice, despite their demanding schedules.

I extend my deepest appreciation to our former lab manager, Mr. Jose Oca-Cossio, who has been through this thesis with me from start to finish, guiding me at every step. His technical help and generous personality has been indispensable to me, and I thank him for always believing in me no matter what. My labmates have always been there for me, whether it was to create a healthy environment for research in the lab, or to simply extend a helping hand or a kind word during my time with them. The lab had become my second home during my busiest months. It would not have been the same without Bettina's words of wisdom and inspiration, Adam's infectious enthusiasm

and endless banter and Matt's kind personality and the swag factor he brought to the workplace.

I thank Dr. Brian Sorg, my former Cancer Biology professor, for his technical advice in the nascent stage of this research. Our correspondence helped me develop a better understanding of tumor phantoms.

I'd also like to acknowledge Mr. Joseph A. Shalosky, the Machine Shop Supervisor of the Chemistry Department for helping me in building the brace for the flow vessel.

My time at UF would have been lacking in great memories had it not been for my closest friend here, Radhika. Her energy, enthusiasm and endless drama kept me going through all the stress and work I put into this thesis. I will be forever grateful to her for her love and support as a true friend. I'd also like to thank my roommates Amrutha, Rachna and Nalanda for being so understanding and putting up with my antisocial tendencies whenever there was work to be done.

My sincere gratitude goes out to you all, and there are many more I haven't acknowledged for lack of space, but who have been instrumental in their enduring support and who have contributed to my success in one way or another.

TABLE OF CONTENTS

	<u>page</u>
ACKNOWLEDGEMENTS	4
LIST OF TABLES.....	8
LIST OF FIGURES.....	9
LIST OF ABBREVIATIONS.....	10
ABSTRACT	11
CHAPTER	
1 INTRODUCTION	13
Rationale behind This Study	13
Objectives.....	14
2 BACKGROUND AND SIGNIFICANCE	15
The Concept of Magnetism and Magnetic Nanoparticles.....	16
The Magnetic Properties of MNPs	17
Advantages of using Iron Oxide Nanoparticles for MFH studies.....	24
History of Hyperthermia for Cancer Treatment	24
Magnetic Fluid Hyperthermia Treatment.....	26
Safety Parameters for <i>In Vivo</i> Studies of MFH	27
Factors for Consideration In MFH Therapy	27
Progress in Hyperthermia Treatment with an Emphasis on Blood-Tissue Perfusion	29
Previous Work on Modeling Heat Transfer in Porous Media for Tumor Perfusion Studies.....	30
3 MATERIALS AND METHODS	33
Design Criteria	33
Preparation and Optimization of Tumor Phantom	34
Materials Tested as Tumor Phantoms.....	34
Desirable Properties of Biocompatible Tissue Polymer Scaffolds	34
Synthesis of the Superporous Hydrogels	35
Design of the Flow Phantom System and Experimental Setup.....	36
Characterization and Visualization of the IONPs	39
Quantification of Iron (III) Oxide in the SPHs	40
Preparation of Tumor Phantom containing the IONPs	40
Spectrophotometric Estimation of IO Content in the IONP-SPHs.....	40
Simulating MFH in IONP-SPHs under Varying Flow Conditions.....	42

4	RESULTS AND DISCUSSION	44
	Specifications and Design of the Flow Vessel	44
	Synthesis and Optimization of the SPHs	46
	Rejection of Several Materials Tested as Tumor Phantoms.....	46
	Optimization of the AM/AA ratio of the Superporous hydrogels.....	47
	Characterization and Visualization of the IONPs	50
	Development of a Novel Method of Entrapment of the IONPs into the SPHs	51
	Optimization of 0.4/0.6 AM/AA Polymer as the Tumor Phantom	55
	Quantification of the IONP Concentration in the 0.4/0.6 SPHs	56
	Visualization of the Superporous Hydrogels and IONP-Superporous Hydrogels....	57
	Heating curves of IONPs under Varying Flow Conditions.....	58
	Challenges encountered while Simulating Physiological Conditions	59
	Physiological Temperature.....	59
	Blood-Mimicking Medium	60
5	CONCLUSIONS	62
6	FUTURE DIRECTIONS	64
	LIST OF REFERENCES	65
	BIOGRAPHICAL SKETCH.....	71

LIST OF TABLES

<u>Table</u>		<u>page</u>
2-1	Magnetic susceptibility ranges of magnetic materials.....	19
2-2	Progress in hyperthermia treatment over the years.....	26
4-1	Comparison of properties of candidates for tumor phantom.....	47
4-2	The swelling ratios of the 0.2/0.8 AM/AA SPHs after the 3-day swelling period.	50
4-3	Flow rates in 0.5/0.5 AM/AA and 0.4/0.6 AM/AA SPHs.....	50
4-4	Temperature (T) readings of the IONP-SPHs at different initial temperatures....	60

LIST OF FIGURES

<u>Figure</u>		<u>page</u>
2-1	Biomedical applications of magnetic nanoparticles.	15
2-2	Magnetic behavior in magnetic materials.	22
3-1	Position of the flow vessel inside the magneTherm™ chamber with the required auxiliary connections in place.	38
3-2	Experimental setup.	38
4-1	Schematic of the designed tumor flow phantom vessel.	45
4-2	The flow vessel with the tumor phantom, attached to a brace to hold it inside the magneTherm™ chamber.	46
4-3	Swelling trend of 0.2/0.8 AM/AA polymers with increasing pH values.	49
4-4	SEM images of the IONPs.	51
4-5	Development of a Novel Method of Entrapment of the IONPs into the SPHs.	52
4-6	Comparison of IONP uptake methods using the final temperature attained by the SPHs in 1 hour.	54
4-7	Concentration trends of the 0.5/0.5 and 0.4/0.6 AM/AA IONP-SPHs over the 3 day-swelling period.	54
4-8	Heating trends of the 0.5/0.5 and 0.4/0.6 IONP-SPHs over the 3 day-swelling period	55
4-9	Comparison of the swelling of the 0.5/0.5 and 0.4/0.6 AM/AA control SPHs and IONP-SPHs after the 3-day swelling period.	56
4-10	SEM images of the 0.4/0.6 SPHs at various magnifications.	57
4-11	Heating trends of 0.4/0.6 AM/AA IONP-SPHs under varying water flow conditions	59
4-12	Effect of saline flow on volume of IONP-SPH.	61

LIST OF ABBREVIATIONS

AA	Acrylic acid
AM	Acrylamide
APS	Ammonium persulfate
BIS	N,N ₀ -methylenebisacrylamide
DI	De-ionized
DLS	Dynamic Light Scattering
ICP-MS	Inductively coupled plasma mass spectrometry
IONP	Iron(III) oxide nanoparticle
IPN	Interpenetrating Polymer Network
MNP	Magnetic nanoparticles
PEI	Polyethyleneimine
PVDF	Polyvinylidene fluoride
SEM	Scanning Electron Microscopy
SPH	Superporous hydrogel
TEMED	N,N,N ₀ ,N ₀ -tetramethylethylenediamine

Abstract of Thesis Presented to the Graduate School
of the University of Florida in Partial Fulfillment of the
Requirements for the Degree of Master of Science

A PERFUSED TUMOR FLOW PHANTOM FOR IRON OXIDE MAGNETIC
NANOPARTICLE-MEDIATED HYPERTHERMIA STUDIES

By

Jolin Philentha Rodrigues

December 2013

Chair: Jon Dobson

Major: Biomedical Engineering

Targeted magnetic fluid hyperthermia (MFH) is a promising cancer therapy that achieves localized tumor heating which selectively destroys tumor cells while limiting side effects. This is achieved through the use of magnetic nanoparticles (MNPs) that are targeted to the tumor tissue which strongly couple to an applied alternating magnetic field (AMF) and produce heat through relaxation losses. Till date, there has been no satisfactory physical tumor phantom to study heat losses by blood perfusion during MFH. Here, a perfused flow phantom for MFH was studied *in vitro*, using a superporous hydrogel of poly(acrylamide-co-acrylic acid)/polyethyleneimine interpenetrating polymer network (P(AM-co-AA)/PEI IPN) to mimic tumor tissue. A new method for the entrapment of Iron (III) oxide nanoparticles (IONPs) in the tumor phantom was developed and optimized for varying concentrations.

A flow vessel was designed to hold the tumor phantom and fit in the chamber of a nanoTherics MagneTherm™ radiofrequency coil device which induced an AMF in the chamber. The AMF generated caused the IONPs to attain hyperthermic temperatures over a period of 60 minutes. The system was tested by monitoring temperature rise in the phantom under varying water flow conditions to replicate blood-tissue perfusion.

Preliminary data acquired showed that blood flow perfusion does not seem to have a significant effect on MFH in targeted tumor tissue; at the iron oxide concentrations tested and flow conditions simulated; but further tests are required to study this. This model holds considerable promise for use in determining optimum heating parameters for the treatment of tumors with MFH.

CHAPTER 1 INTRODUCTION

The International Agency for Research on Cancer (IARC) reported that in 2008, 12.7 million new cancer cases and 7.6 million cancer deaths were reported globally¹. Since cancer is a potentially malignant disease that has a host of external and internal contributing factors, which cumulatively compound the disease over a period of many years, the problem of cancer is a formidable force to be reckoned with.

MFH is a promising cancer treatment therapy that has fewer side effects as compared to other cancer treatment modalities like chemo- and radiotherapy, and could potentially be used as an adjuvant to these therapies to increase the overall efficacy of the treatment. MFH is the targeted localization of MNPs to the tumor tissue, introduced via various modes like direct injection or antibody targeting. The targeted tissue is made to heat up by heat relaxation losses upon the application of an AMF. This leads to direct breakdown of the essential chemical and mechanotransductive pathways in cancer cells, leading to apoptosis.

Rationale behind This Study

The current treatment modalities like radio- and chemotherapy offer limited selectivity for cancer cell targeting and subsequently a large portion of healthy tissue is affected as well. This in turn leads to collateral organ damage and sub-optimal deposition of the therapeutic agent in tumors. MFH has the potential to address these shortcomings through advantages such as; (i) having fewer deleterious side effects, (ii) the potential to reach the less-accessible tumor core and not just the tumor periphery, (iii) the IONPs have low toxicity in therapeutic doses, and (iv) repeated hyperthermia treatments are possible without further dosing or corporeal invasion if the particles

remain *in situ* and are not retrieved, excreted or broken down immediately following treatment¹.

The heating ability of tumors is highly influenced by the blood flow conditions and experiments have proved that poorly perfused areas are more heat-sensitive due to hypoxia, acidosis and energy depletion, rendering MFH more effective in tumors than healthy cells². However, the local tissue cooling effect of blood flow may cause problems with the heat deposition, possibly rendering MFH ineffective if the blood flow contributes to the thermal decay by conduction and perfusion. Some experimental and theoretical models³⁻⁷ have been designed to study the effects of blood flow, but this thesis aims to develop a physical tumor flow perfusion phantom where the microvasculature of the tumor is accounted for.

Objectives

The overall goal of this research was to develop an easy to use blood perfusion flow phantom to study the heating effects of MFH *in vitro*, in order to determine the heating parameters for use in MFH applications. The following objectives supported the main goal:

1. To design and fabricate a flow vessel for MFH.
2. To develop an effective phantom of tumor tissue that mimics physiological blood flow under MFH.
3. To create a novel method that enables controllable loading of IONPs at desired concentrations in the tumor phantom.
4. To test the performance of this newly created system by simulating MFH under fluid flow to simulate heat transport by blood.

CHAPTER 2 BACKGROUND AND SIGNIFICANCE

Magnetic micro- and nanoparticles are increasingly being used in biomedical applications. The emerging field of biomedical nanomagnetism has progressed much in the past decade, due to the unique properties of magnetic nanoparticles (MNPs). These have developed into innovative tools of translational research in the fields of materials science, biotechnology, molecular biology, and engineering, besides others. Some of the biomedical applications of MNPs are: targeted drug/ gene delivery and triggered release⁸⁻¹¹, nanomagnetic actuation¹²⁻¹⁶, magnetic separation of labeled biological entities^{17, 18}, contrast agents for Magnetic resonance imaging (MRI)^{19, 20} and Magnetic particle imaging (MPI)^{8, 21-24}, magnetic fluid hyperthermia (MFH)^{25, 26}. Fig. 2-1 displays at a glance the various biomedical applications of magnetic nanoparticles.

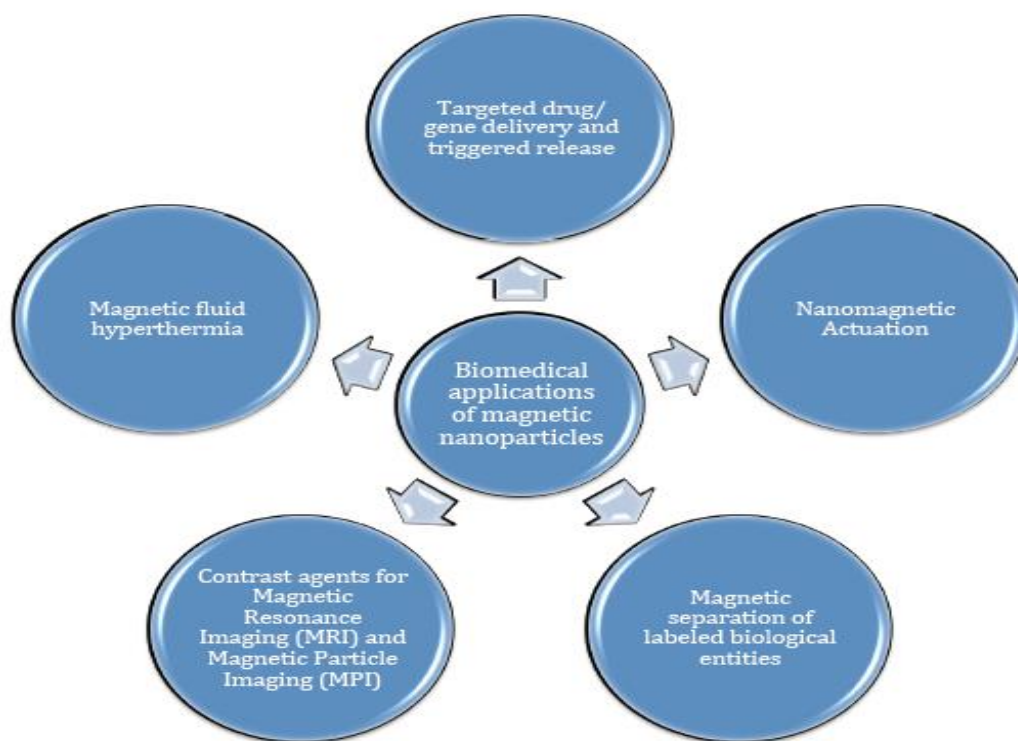


Figure 2-1. Biomedical applications of magnetic nanoparticles.

MFH is the controlled heating of targeted tumor tissue using suspended magnetic nanoparticles (usually IONPs) to treat malignant cancers while sparing healthy tissue. This works by locally elevating the temperature of the tissue to 42-46°C for 30 minutes or more ²⁵.

The MFH cancer treatment modality, its limitations, and the latest progress in the field, especially with respect to blood- tissue perfusion, will form the focus of the later sections of this literature review. In order to understand MFH, we must briefly explore concepts in magnetism and magnetic materials.

The Concept of Magnetism and Magnetic Nanoparticles

Magnetism refers to the intrinsic property of certain materials which attract or repel similar materials. Every magnet has 2 poles- north and south. Opposite poles attract and similar poles repel. This phenomenon is exhibited by magnetic materials like iron, nickel, cobalt, gadolinium and dysprosium.

MNPs are mostly spherical particles of less than 100 nm in diameter that are composed of elements like iron, nickel, cobalt and their oxides ²⁷. Since nanoparticles are at sizes comparable to those of some biological entities (a cell is around 10 microns in size, while proteins and membrane structures are in the nm to 10's of nm range), they can effectively interact with them, hence exploiting them for biomedical applications can be accomplished with unprecedented control ²⁸. Their characteristic magnetism can be remotely manipulated by alternating magnetic field gradients, because the body is largely transparent to magnetic fields. Nanomagnetic particle technology has recently come to the forefront of cancer research due to the cutting-edge approaches it offers as an alternative or adjuvant to conventional diagnostics and therapy.

At nanoscale dimensions (of the order of a few nm to 100's of nm), high surface-to-volume ratios can be accomplished for the efficient transport of MNPs in biological fluids, which will be discussed in a later sub-section. MNPs typically consist of magnetic cores coated with stabilizing shells that serve as surfaces for functionalization, i.e. it allows their tagging with biological ligands targeted to specific cell receptors²⁹. They are usually artificially engineered and have numerous tailored properties like size, shape, polymer coating and functionalization.

The Magnetic Properties of MNPs

Every magnet exists as a dipole, i.e. with a north pole on one end and south pole on the other. A magnetic dipole experiences a torque if placed in a magnetic field perpendicular to it, which is called the magnetic moment m . In quantum mechanics (at the sub-atomic scale), magnetic effects originate from the spin and orbital moments of the electrons.

Atomic orbitals are mathematical functions that quantify the probability of the existence of an electron or electron pair around the nucleus. Uncompensated spin moments dominate the magnetic effect. Iron being a transition series element, has uncompensated spins in the 3d orbital, which gives rise to its “spin” magnetic moment, aligned parallel to the applied field. The magnetization of a material in an external magnetic field is described by the magnetization vector \mathbf{M} , the dipole moment (m) per unit volume (v). It aligns in the direction of the applied field of strength H and is given by:

$$\mathbf{M} = \chi \mathbf{B} \quad (2-1)$$

In Ampere/metre, where χ is known as the *magnetic susceptibility* of the medium. It is a dimensionless constant independent of temperature. It is assigned to a material as a characteristic value of its magnetizability.

The magnetic induction and electromagnetic force experienced by magnetic materials are also crucial to understanding how magnetism works. When a field of strength H is applied to a magnetic material, the magnetic induction is given by:

$$\mathbf{B} = \mu_0 (\mathbf{H} + \mathbf{M}) \quad (2-2)$$

In Tesla, where μ_0 = permeability of free space.

The electromagnetic force \mathbf{F} induced in a moving test charge by a magnetic field in the presence of an external electric field is given by the Lorentz force law³⁰:

$$\mathbf{F} = q (\mathbf{E} + \mathbf{v} \times \mathbf{B}) = q\mathbf{E} + q\mathbf{v}B \sin \theta \quad (2-3)$$

In Volts, where q = charge, \mathbf{E} = electric field vector, \mathbf{v} = velocity vector, \mathbf{B} = magnetic flux density vector and θ = angle between the two vectors.

Types of magnetism. There are 3 main types of magnetism in magnetic materials, based on electronic configuration: Diamagnetism, Paramagnetism and Ferromagnetism. Their properties are elucidated as follows:

1. **Diamagnetism.** There are no uncompensated electron spins, hence they respond very weakly to magnetic fields, i.e. they are repelled by both poles of a magnet). and they are weakly repelled by applied magnetic fields (weak, negative magnetic susceptibility χ). Most biological materials are diamagnetic.
2. **Paramagnetism.** There are uncompensated electron spins in the material. χ follows a linear inverse temperature dependency for paramagnets, i.e. it decreases with increasing temperatures. Paramagnets are weakly attracted to both poles of a magnet and their magnetic moments align to some degree (net magnetization effect) only in the presence of an external applied magnetic field. The best-known examples of paramagnetic materials are the ions of some transition elements and rare-earth elements²⁶.

3. **Ferromagnetism.** Ferromagnets have individual coupled, uncompensated spin magnetic moments. In ferromagnets, the variation of χ is different above and below a certain critical temperature called the *Curie temperature*. The quantum mechanical coupling of spin moments in ferromaterials break down at this temperature. They are strongly attracted to the magnetic poles and retain their magnetization even when the external magnetic field is removed, i.e. they exhibit *hysteresis*. Examples include lodestone (magnetite or Fe_3O_4) and hematite (Iron (III) oxide or Fe_2O_3)²⁶.

Table 2-1. Magnetic susceptibility ranges of magnetic materials.

Type of magnetism	χ	Examples	Reference
Diamagnetism	Weak, negative χ , of the order -10^{-6} to -10^{-5}	Ionic crystals and inert gas atoms	31
Paramagnetism	Moderately strong, positive χ of the order 10^{-5} to 10^{-2} .	Ions of transition elements and rare-earth elements	31
Ferromagnetism	Strong, positive χ , of the order 10^3 to 10^6	Lodestone and hematite	31

Domains in magnetic materials. Below the Curie temperature, ferromagnets are characterized by *spontaneous magnetization* and are composed of small regions called *domains* within the material, each having its own magnetic moment wherein the atomic dipoles are linked together in a single direction. However, the magnetic moments of the individual domains are oriented randomly to each other in order to minimize magnetostatic energy, only aligning under the influence of an external magnetic field. The alignment of the domains to the applied field increases with the field strength until it reaches *saturation magnetization* (M_s), beyond which there is no increase in magnetization despite increasing H .

In tiny particles of magnetite (the size varies for different materials and is a material property dependent on the spin configuration), the spins are aligned in the same direction resulting in uniform magnetization and is called single domain (SD)³². In

larger particles the material exists in multiple domains (MD) having distinctly non-uniform states of magnetization to minimize its internal energy³². The net amount of energy reduced as a result of creating multiple domains in the material is a trade-off between the magnetic field energy saved, the magnetocrystalline energies and the exchange energy expended to create the domain walls demarcating the domains. The alignment of the domains in the various types of magnetic materials can be seen in Fig.2-2.

Special cases of ferromagnetism. 3 unique cases of ferromagnetism showing ordered magnetism are described here: antiferromagnetism, ferrimagnetism and superparamagnetism.

1. **Antiferromagnetism.** These materials do not have a net magnetization usually, as their uncompensated spins are coupled anti-parallel to neighboring spins. However, a net magnetization can be seen in some materials like hematite. Above a certain higher temperature called Néel temperature, this ordered magnetism disappears and is replaced by paramagnetic behavior. Ex: A biological example is ferrihydrite.
2. **Ferrimagnetism.** In ferrimagnetic materials, the uncompensated spins are coupled anti-parallel to each other, like in antiferromagnetism. The opposing moments, however, are unequal and give rise to a relatively strong net spontaneous magnetization. Ex: The oldest-known magnetic substance, magnetite (Iron(II,III) oxide; Fe_3O_4), is a ferrimagnet.
3. **Superparamagnetism.** Superparamagnets (SPMs) may be ferro-, ferri- or antiferrimagnetic. In these particles, though the spins are coupled, the energy required to flip the magnetization between energy minima is lower than the available thermal energy. The spin-flip barrier is given by $M_s \cdot a^3$, where M_s = saturation magnetization and a =length. The relaxation time τ is the time between reversals of magnetic moment direction due to thermal fluctuation and is given by the Néel-Arrhenius equation³³ that governs superparamagnetism:

$$\tau_N = \tau_0 \exp(KV/k_B T) \quad (2-4)$$

Where τ_0 = attempt time = 10^{-9} – 10^{-10} s, characteristic of the material, K =anisotropy energy, V =volume, k_B = Boltzmann's constant = $1.38 \times 10^{-23} \text{ m}^2 \text{ kg s}^{-2} \text{ K}^{-1}$, T =temperature. Fig.2-2 shows the exponential dependence of T on the energy barrier KV at measurement time of around 100 s. Superparamagnetism depends on particle size and

measurement time ²¹. Ferrofluids are excellent examples of superparamagnets in colloidal suspension.

M-H curves. The magnetic “memory”, or residual magnetism, of a ferromagnetic material enables it to retain the magnetization M induced in it by a magnetic field of strength H , even after its removal. This is due to the presence of magnetic domains (or single domains as in the case of SPMs), that align their moments according to the direction of the applied field. After reaching M_s , the magnetization relaxes back to zero upon the application of the field in the opposite direction. This property of magnetic irreversibility in ferromagnetic materials is used to plot M as a function of H , creating M-H curves, as shown in Fig.2-2. The area of the hysteresis loop relates to the amount of energy dissipated upon reversal of the field. The coercive force, H_c (Ampere/metre) is the magnetic field strength required to drive the M to zero after M_s has been attained. Thus coercivity measures the resistance of a ferromagnetic material to becoming demagnetized. High coercivity leads to magnetic hardness and low coercivity to magnetic softness of the ferromagnet.

MNPs have the characteristic property of converting electromagnetically induced energy into heat, which is the underlying principle behind their application in tumor hyperthermia. The amount of heat generated per unit volume in FM heating is given by the product of the AC field frequency f and the area of the hysteresis loop:

$$P_{FM} = \mu_0 f \int H dM \quad (2-5)$$

Where, P_{FM} is the measured heating power per unit length under the AMF and $\int H dM$ is the area of the hysteresis loop.

For Superparamagnetic heating, the corresponding heat generation formula is given by Rosensweig’s equation ³⁴ :

$$P_{\text{SPM}} = \mu_0 \pi \chi'' f H^2 \quad (2-6)$$

Where P_{SPM} = measured heating power per unit length under the AMF for SPM particles and χ'' = frequency-dependent lag component of complex susceptibility of the SPM material. Fig.2-2 displays the M-H curves in different cases of magnetic behavior.

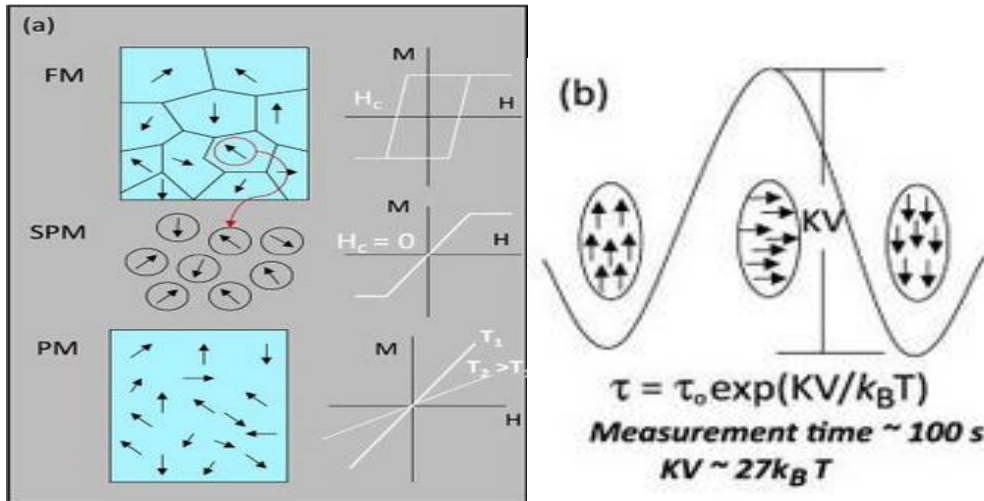


Figure 2-2. Magnetic behavior in magnetic materials. A) Magnetic domains and hysteresis curves in ferromagnets (FM), superparamagnets (SPM) and paramagnets (PM), B) Exponential dependence of τ on the energy barrier KV at measurement time of around 100 s, in SPMs. (adapted from Krishnan, KM. 2010. Biomedical Nanomagnetism: A Spin Through Possibilities in Imaging, Diagnostics, and Therapy (Figure 2a) and 2b)). © 2010 IEEE Trans Magn.).

Hyperthermia heating mechanisms. When exposed to AMFs, there are four mechanisms for heat transfer via MFH:

1. **Eddy currents.** Currents are induced in the conductor by changing magnetic fields. These are negligible in nanoparticles due to their small size and low electrical conductivity.
2. **Hysteresis heating.** Hysteresis losses are negligible in ferromagnetic nanoparticles due to the relatively weak fields applied. Magnetically blocked MNPs are only cycled through minor hysteresis loops and superparamagnetic particles do not exhibit hysteresis.

3. **Néel relaxation.** This is the rotation of the magnetization vector of the particle due to the electron spins as it attempts to follow the changing magnetic field direction. This is the major source of energy deposition in superparamagnetic particles exposed to AMFs (see Eq. 2-4 & 2-6)
4. **Brownian relaxation.** In colloids of magnetically blocked MNPs that are exposed to an AMF, Brownian rotation/relaxation³⁵ occurs due to rotational reorientation of the particle as it follows the changing field vector. This is the major source of energy deposition for magnetically blocked particles as given by Eq.2-7:

$$\tau_B = 4\pi\eta r_h^3 / (k_B T) \quad (2-7)$$

Where τ_B = Brownian relaxation time, r_h = hydrodynamic radius of the particle.

The dominant mechanism of heat transfer due to relaxation will be the faster of the two mechanisms (which is Néel relaxation for SPMs), and is given by an effective relaxation time defined by:

$$\tau_{\text{eff}} = \tau_N \tau_B / (\tau_N + \tau_B) \quad (2-8)$$

In hyperthermia experiments, the Specific Absorption Rate (SAR) is used to the amount of energy transferred to the particles by the AMF³⁶:

$$\text{SAR} = C \left(\frac{\Delta T}{\Delta t} \right)_i \cdot \left(\frac{m_i}{m_p} \right) \quad (2-9)$$

In W g^{-1} , where C =Specific heat capacity of water= 4.186 Joules/gram °C, $(\Delta T/\Delta t)_i$ = initial gradient of the heating curve (temperature vs. time) (°C/s), m_i = mass of the sample (g), m_p =mass of the MNPs in the sample(g).

Due to the difficulty in comparing SARs from different hyperthermia experiments, another parameter, the Intrinsic Loss Parameter (ILP)³⁷, has been established to determine the reproducibility of the results from different frequencies and field strengths. It is given by:

$$\text{ILP} = \text{SAR} / H^2 f \quad (2-10)$$

Advantages of using Iron Oxide Nanoparticles for MFH studies

The most commonly used magnetic nanoparticles for biomedical applications are ferrimagnetic iron oxides- Iron (III) oxide or maghemite ($\gamma\text{-Fe}_2\text{O}_3$) and Iron (II,III) oxide or magnetite (Fe_3O_4). There are several distinct advantages of using iron oxide nanoparticles (IONPs) for hyperthermia:

- **Biocompatibility.** IONPs are biocompatible to a certain extent, but relatively high amounts have been shown to cause tissue damage. The minimum iron oxide concentration shown to cause tissue damage in the liver is 4.5 mg per g wet weight³⁸. Hence, when used for biomedical applications, they are first coated with a biocompatible, stabilizing coating. This coating helps in preventing cytotoxicity and also serves as a means of functionalizing the IONPs by targeting them to specific receptors on tumor cells, a quality that is crucial when the IONPs are injected into the bloodstream directly.
- **Enhanced Permeation and Retention effect (EPR).** Tumor microvasculature is highly permeable due to their abnormal morphology. Furthermore, the IONPs are also prevented from being cleared by the Reticulo-Endothelial System (RES), due to the inefficient tumor lymphatic system. This allows the IONPs of sizes between 10 and 100 nm to selectively accumulate in tumors²¹. This EPR effect can be enhanced through coating of the IONPs. This includes binding hydrophilic polymer chains to prevent opsonization (binding and removal by the immune response agents)³⁹, altering their bulk properties like reducing particle size⁴⁰, and creating topographical variations on the surface⁴¹.
- **Easy synthesis methods.** IONPs are fairly easy to synthesize by facile and established methods like co-precipitation and thermal decomposition^{27, 42, 43}
- **High magnetization.** The stronger magnetic signal of IONPs over that of the hemoglobin Iron in the biological tissue results in their easy detection²⁹.
- **Minute quantities.** SPMs have high magnetization (high SAR) and do not have dipole interactions (especially if they are coated) to cause aggregation. They can therefore be used in minute quantities to achieve the same effect as using greater quantities of MNPs with lower SAR values^{21, 32, 44, 45}.

History of Hyperthermia for Cancer Treatment

Cancer is the collective term for the group of diseases caused by the abnormal, uncontrolled multiplication of living cells in the body. According to the World Health

Organization, “Worldwide, one in eight deaths is due to cancer; cancer causes more deaths than AIDS, tuberculosis, and malaria combined”⁶⁶.

“Give me the power to produce fever and I will cure all diseases”- Parmenides (ca. 540 – ca. 470 B.C.). As early as 3000 B.C., the Roman, Greek and Egyptian civilizations elevated body temperatures to rapidly destroy cells in breast cancer treatments, using tools like hot metal blades. Ancient Indian and Chinese civilizations also used regional and whole-body heat treatments to cure certain lesions, what we now refer to as cancer. These treatments involved the application of direct heat to ablate tumor cells which results in their crude destruction. They did not involve the controlled application of heat to elevate body temperatures to 5-9°C higher than normal body temperature for therapeutic purposes, which is commonly known as hyperthermia (*hyper*=rise, *therme*=heat) today^{46, 47}. Several significant contributions to hyperthermia research are summarized in Table 2-2.

As a result, in the later part of the 20th century, systemic hyperthermia treatment for cancer (later coined as “oncothermia”) regained prominence, and clinical trials for whole-body hyperthermia treatment are being currently undertaken at several centers in the United States, Europe, Japan and China.

Scientific progress in novel fields like nanoparticle technology and MFH is gaining worldwide attention in the field, and holds substantial promise in cancer therapy. MFH, with the focus on blood-tissue flow perfusion in tumors, will be described in the next section.

Table 2-2. Progress in hyperthermia treatment over the years.

Year	Researcher	Contribution to hyperthermia	References
1866	C. D. Busch	First reported therapeutic effects of hyperthermia	48
1893	W. Coley	Treatment of inoperable cancers using high fevers induced by the injection of Coley's toxins	49
1881	J. d'Arsonval	Introduced autoconduction- high-frequency currents (350-450 mA) to treat various diseases	50
1927	N. Westermark	Proposed a temperature of 40-45°C to heat tumor tissue due to their higher heat-sensitivity over healthy tissue	51
1962	G. W. Crile Jr.	Discovered controlled temperatures of 42-50°C could selectively destroy tumor tissue while sparing healthy tissue	48
1971	A. Westra and W.C. Dewey	Performed first hyperthermia experiment on mammalian cells at controlled temperatures above 40°C;found that above 42.5°C, slight increase in temperature causes notable reduction in cell mortality	52
1973	H.A. Johnson and M. Pavelec	Combined hyperthermia and chemotherapy treatments enhance cytotoxicity of drugs to treat mammalian tumors	53

Magnetic Fluid Hyperthermia Treatment

Recent developments in the field of biomedical nanomagnetism have highlighted the role of nanomagnetic particles in “theranostics”(integrated therapeutic and diagnostic technologies), that may play a key role in personalized medicine, the need for which is growing in view of increasing susceptibility to cancer, together with the increasingly complicated disease profiles of patients. IONPs have been traditionally used for diagnostic purposes (MRI) and are now being intensively studied as vectors for hyperthermia in cancer therapy.

Safety Parameters for *In Vivo* Studies of MFH

In 1957, in the first experiment of its kind, Gilchrist et al.⁵⁴ carried out selective inductive heating of lymph node tumors using iron oxide ($\gamma\text{-Fe}_2\text{O}_3$) magnetic particles of size 20 to 100 nm. This study demonstrated the feasibility of inducing desirable differential heating of tumors in the human body using IONPs. Safe limits for inductive heating of tissues by IONPs were shown to be tolerable by biological tissue at any combination of field strength (H) and frequency(f) according to the fixed value³⁷ of $H \cdot f = 4.85 \cdot 10^8 \text{ A} \cdot \text{m}^{-1} \cdot \text{s}^{-1}$, for hyperthermia of tumors in the body torso. f can range from 0.05-1.2 MHz and H from 0-5 kA m^{-1} for medical applications³⁷. For hyperthermia in the body extremities however, a slightly higher value of induction field strength can be permitted^{55, 56}. These limits however, have been shown to be of limited value, and have not been extensively studied. Furthermore, use of IONPs in hyperthermia applications has been found to have no significant detrimental effects in biological tissues in therapeutic amounts, being cleared via various routes^{44, 57}.

Factors for Consideration In MFH Therapy

These considerations can be classified as physiological, hydrodynamic and physical:

1. **Physiological factors.** a) opsonization of the IONPs and subsequent clearance by the RES, as mentioned in Chapter 2, b) non-specific binding to receptors on healthy cells, c) transport constraints posed by interfering vasculature and tissue (like the blood-brain barrier). These can be overcome by functionalization of the IONPs.
2. **Hydrodynamic factors.** a) osmotic pressure gradients which interfere with the localized delivery of the IONPs and/or drugs to the tumors; and b) blood and nutrient supply that influence the bioavailability.
3. **Physical factors.** The physical factors that need to be considered are the coupling of the IONPs to the field, energy-heat conversion and the scale of this conversion in small particles.

4. **Blood-tissue perfusion.** A major consideration for MFH is the counteraction of the heating by blood-tissue perfusion of the tumor microenvironment. Experimental studies have shown that only 20%-85% of tumor microvessels are perfused at a given time². Their chaotic vasculature, irregular branching patterns, lack of smooth muscle cells and endothelial cells, and a poorly functioning lymphatic drainage system all contribute to the high interstitial pressures (IFP) in tumors (as high as 45 mm Hg)⁵⁸. This high IFP also results in lowered uptake of anti-cancer agents⁵⁹, in this case, IONPs, preventing optimal heat deposition.

The magnetic properties of the IONPs can be unsuitable for use in hyperthermia due to factors like their large size and instability in biological fluids, leading them to be threatened by the body's defense system. Hence their size and surface chemistry need to be tailored to their specific application. The challenges to localization of IONPs for hyperthermia strategies can be overcome by avoiding RES and increasing the circulation time in the blood system by tailoring the size, surface charge and surface modification of the IONPs, using polymeric, liposome coatings (like polyethylene glycol or PEG) to maintain the stability of the IONPs in the body. Also, as mentioned in an earlier section, the EPR effect of the heterogeneous, highly permeable tumor microvasculature facilitates the accumulation and retention of the IONPs (sizes between 10-100 nm) in the tumor tissue, which is the underlying strategy for MFH²¹.

Typical perfusion rates are between 5-15 mL min⁻¹ per 100 g of tumor tissue²¹. To attain therapeutic temperatures, Specific Heat Power (SHP) must be between 20 and 40 W kg⁻¹ in the targeted region, and the heat dissipation by the flowing blood must be factored into the therapy²¹. This thesis investigated the effects of heat dissipation by blood flow in an *in vitro* model system for MFH. A tumor model was designed incorporating the tumor microvasculature and simulating blood flow through the system to study the effect of blood-perfusion cooling effects on hyperthermia.

Progress in Hyperthermia Treatment with an Emphasis on Blood-Tissue Perfusion

Since the inception of the concept of magnetically-mediated hyperthermia around 50 years ago, the field has evolved into four sub-classes: (i) arterial embolization hyperthermia (AEH), (ii) direct injection hyperthermia (DIH), (iii) intracellular hyperthermia (IH) and (iv) interstitial implant hyperthermia (IIH), all using ferromagnetic particles as mediators of hyperthermia¹. A number of studies have successfully administered therapeutic hyperthermia in pre-clinical models⁶⁰⁻⁶².

In 2001, Otsuka et al.⁶³ reported hyperthermia treatment of soft tissue sarcomas in combination with radio- and chemotherapy. The results led them to conclude that 98% of patients showed significant reduction in the tumors. Other studies also reported the safety and efficacy of these therapies in combination with each other^{64, 65}.

AEH deals with the passive transportation of the nanoparticles to the tumor through its arterial supply, followed by AMF exposure. This technique uses the EPR effect and high permeability of the tumor microvessels to concentrate the nanoparticles in the tumor. A study by Moroz et al.⁶⁶ in 2001 carried out on hepatic VX2 carcinomas in rabbits demonstrated the heating up of large tumors at nearly double that of small tumors in an AMF of $H = 45 \text{ kA m}^{-1}$ and $f = 53 \text{ kHz}$, due to the relatively better heat conduction and poorer cooling mechanisms within the necrotic regions of the larger tumors as compared to the smaller tumors.

DIH, IH and IIH deal with the active targeting or functionalization of either locally or systemically administered nanoparticles with antibodies that are tailored to bind to the targeted tumor. Immense progress has been made in this area, as well as that of

multifunctional nanocarriers and optimized core-shell nanoparticles over the past ten years^{18, 67}.

Magnetic fluid hyperthermia was successfully carried out for the first time on pre-irradiated prostate cancer by Andreas Jordan and his team in 2005²⁵. The direct monitoring of temperatures was accomplished through an intracranial thermometry catheter and compared with previously measured temperatures from the density distribution of the nanoparticles, SAR values and the estimated perfusion at the tumor area. An increase in survival from 6.2 months to 13.4 months was observed as compared to previous radio- and chemotherapy treatments.

In 2011, Matsumine et al.⁶⁸ first reported the hyperthermia treatment of metastatic bone lesions using a direct application of an AMF to the affected limb, with the surgical implantation of naked magnetite IONPs and a bone substitute- calcium phosphate. The results indicated that 32% of lesions were reduced and resulted in visible bone formation, 64% showed no progressive lesions for more than three months and just 4% presented a poor outcome, suggesting the high feasibility and effectiveness of hyperthermia and comparable results with radiosurgery therapy.

These studies have significantly impacted the field of MFH by affirming its scope and feasibility in cancer therapy.

Previous Work on Modeling Heat Transfer in Porous Media for Tumor Perfusion Studies

It is complicated to run *in vivo* hyperthermia experiments, more so in human patients, and technically challenging to replicate the physiological conditions *in vitro*. Hence, in addition to *in vitro* and *in vivo* studies, a number of theoretical studies of

magnetic hyperthermia considering tumor blood perfusion have also been performed, which also include the modeling of heat transfer in porous material.

Hilger et al.⁶⁹ in 2002 compared the heating potential of different iron oxide samples suspended in water and agarose gel at $H = 6.5 \text{ kA m}^{-1}$ and $f=400\text{kHz}$. The ferrofluids tested were of hydrodynamic diameters 10 nm, 125 nm, 200 nm and 280 nm. No significant change in SAR values took place for these ferrofluids when suspended either in water or gel, showing there was no significant correlation between the SAR and the particle suspension medium. Out of these ferrofluids, the coated MNPs having 10 nm hydrodynamic diameter had the highest SARs (73-93 W g^{-1}). They found that the SAR values showed different trends for both samples in gel suspensions, i.e. they reduced significantly for the ferromagnetic particles of large diameters (approximately 350 nm), from 74 W g^{-1} (particle suspensions in water), to 8 W g^{-1} (low values for solid agar). Ferromagnetic particles of smaller diameters (100 nm) showed corresponding increase in SAR values from 2 W g^{-1} in water to 8 W g^{-1} in solid gel. These observations can be attributed to the fact that the uncoated MNPs show decreased heating potential due to Brownian relaxation when immobilized in the agarose gel medium. They concluded that the observations with the larger MNPs reflect the *in vivo* situation of the degree of particle immobilization at the tumor area as the gel was representative of tumor tissue in this study. Additionally, the solid gel matrix concentration was shown to have inconsequential effects on the SAR when the MNPs were uniformly mixed⁴³. These results would be taken into consideration while modeling the tumor phantom.

The main advantage of using porous material to model bioheat transfer in tissue is the use of fewer variables in the model as compared to other bioheat transfer models.

Bioheat transfer models like the one-equation model for porous media can effectively address the problem of non-thermal equilibrium between the blood and tissue, and heat exchange by convection in the blood⁷⁰.

Several researchers^{3, 4} experimentally and numerically^{6, 7} investigated the heat diffusion characteristics of magnetite nanoparticle- dispersed-hydrogels as spherical heat sources. In 1999, Andrä et al.⁷¹ used a similar spherical model (using magnetic microparticles) to mimic breast carcinomas, which they then embedded in cow tissue *in vitro*. They then compared the numerical estimations of heat diffusion characteristics with that of the experimentally derived data and reported a significant agreement between the two datasets.

One of the drawbacks with using these spherical models was that the measurements of heat were limited to those at the surface of the heat source. In order to realistically model a tumor, the flow properties and microvasculature were required to be incorporated into the physical tumor phantom. Therefore, by developing a realistic tumor phantom, these parameters could be accounted for, and subsequently, heat dissipation by blood-tissue perfusion (bioheat transfer).

CHAPTER 3 MATERIALS AND METHODS

Design Criteria

The design of a tumor phantom that successfully mimics physiological flow conditions would incorporate the factors that influence the blood flow and heat dissipation of the tumor tissue under consideration. The criteria for designing a tumor phantom that incorporates these factors are as listed:

1. **Tumor microenvironment.** The tumor microenvironment is different from a microenvironment composed of healthy cells, due to the abnormality of the cancerous cells and disproportionality of the supplying microvasculature. The inadequacy of the blood supply in tumors leads to physiological irregularities, mainly in oxygen supply and pH, which impact the therapeutic efficacy of the hyperthermia treatment modality⁷². The heterogeneity of the microvasculature needs to be accounted for in the design of the tumor phantom. Due to the heterogeneous vasculature in the tumors, blood flow is inhomogeneously distributed and results in low-flow and high flow areas in the tumor tissue, which plays an important role in hyperthermia treatment.
2. **Tumor microvasculature.** The blood vessels are usually of mean diameters around 10 μm (capillaries), 10-225 μm (arterioles) and venules (20-650 μm)⁷³. Hence, these dimensions need to be created in the phantom to simulate the meshwork of interconnected tumor vasculature.
3. **Blood flow.** Typical perfusion rates are between 5-15 mL min^{-1} per 100 g of tissue²¹. The phantom used must be able to enable permeability of the blood-mimicking medium such that the flow rate obtained falls within this range.
4. **Temperature monitoring and heat loss.** The temperature of the tumor phantom also needs to be monitored and heat loss to the surroundings needs to be prevented in order to accurately study the heat dissipation by the simulated blood flow. This will be done by thermally insulating the tumor phantom system.
5. **High temperature stability.** In addition, the phantom will need to be stable at hyperthermic temperatures, hence low melting point- materials cannot be chosen.
6. **Adequate mechanical strength.** The phantom needs to have good mechanical strength so it will maintain its integrity under the pressure conditions induced in the flow system.

Preparation and Optimization of Tumor Phantom

The material selected as the tumor phantom had to satisfy all the above criteria. Preliminary studies used different porous materials which were tested to see if they fulfilled these criteria. The selected material was later developed further and optimized for the purposes of this study.

Materials Tested as Tumor Phantoms

Silica gel, agarose gel, Silica-agarose gel mixture, Sephadex[®] G-10 and G-20 beads, Sephadex[®] - agarose gel mixture and high- and low- melting point agarose gel mixture were among the gels tested for the above characteristics.

Desirable Properties of Biocompatible Tissue Polymer Scaffolds

Biocompatible tissue polymer scaffolds were found to be good candidates for this phantom. A thorough search of the literature yielded one such scaffold- a superporous hydrogel (SPH), namely poly(acrylamide-co-acrylic acid)/polyethylenimine interpenetrating polymer network (P(AM-co-AA)/PEI) IPN⁷⁴. It was tested and seemed like a fitting candidate for the proposed tumor phantom for flow perfusion studies due to the following properties exhibited by it:

1. **Pore size, high water affinity and permeability.** SPHs have pore sizes of 10-1000 μm ⁷⁴ and this range seemed appropriate to mimic the blood vasculature in the tumor tissue. SPHs absorb water fast and have greater than 95% water content. Their interconnected pores present throughout the matrix absorb water at high rates through capillary force. The permeability was tested by running water through the gel by peristaltic pump action, to achieve the desired blood flow rate.
2. **High thermal stability.** The operating temperatures the phantom would be subject to can rise to about 60°C, but the melting point of the SPH is higher (70°C), as tested. Hence, the gel was able to be stable under the operating temperature.
3. **Mechanical strength.** The mechanical strength, i.e. the compressive strength of water-swollen SPHs increased with PEI concentration and decreased with AA

concentration for neutralized samples. Maximum swelling ratio of PEI to monomer was observed around the AA weight fraction of 0.4 for all PEI concentrations. More water uptake due to swelling results in the formation of larger pores leading to swelling stresses that cause the SPH to crack more easily. The optimal AM/AA fraction and PEI concentration would be that which allows the swelling of the SPH to a reasonable limit to allow the development of interconnected pores forming channels, and has good compressive strength.

These properties were tested for different AM/AA concentrations and over different pH ranges.

Synthesis of the Superporous Hydrogels

Chemicals. Acrylamide (AM) (Sigma- Aldrich) and acrylic acid (AA) (Sigma- Aldrich) were used as monomers. N,N'-methylenebisacrylamide (BIS) (Sigma-Aldrich) was used as crosslinking agent, and the redox pair of N,N,N',N'-tetramethylethylenediamine (TEMED) (Sigma-Aldrich) and ammonium persulfate (APS) (Sigma-Aldrich) as initiator. Sodium hydroxide (Sigma-Aldrich) was used as neutralization agent, sodium bicarbonate (Sigma-Aldrich) as blowing agent, Pluronic PF 127 (Invitrogen) as foam stabilizer, and ethanol (Decon) as wetting agent. Highly branched polyethyleneimine (PEI) (Sigma-Aldrich) with the weight average molecular weight of $750,000 \text{ g mol}^{-1}$ was used to form the IPN with the monomer solution of AM and AA.

SPH synthesis. For the AM/AA weight ratio of 0.2/0.8, a monomer aqueous solution was first created, composed of 2 g of 50% (w/v) AM and 8 mL of 50% (w/v) AA. 2.2 mL of 2.5% BIS (w/v) was added, along with 0.4 mL of 20% (v/v) TEMED and 1 mL of 10% (w/v) PF-127. Stock solutions were prepared for different compositions of AM/AA weight ratios of 0.8/0.2, 0.6/0.4, 0.5/0.5, 0.4/0.6 and 0.2/0.8. 15 % PEI aqueous solution was then added to each stock solution to obtain a final PEI/monomer weight ratio of 5/100.

1 mL of the stock solution - PEI aqueous solution mixture was added in a Corning 15 mL polypropylene centrifuge tube for the polymerization. pH was adjusted to 5.0 by adding 50% (w/v) sodium hydroxide aqueous solution, when the system has appropriate viscosity. The sodium hydroxide aqueous solution was added in increments of 50 μL to get an accurate pH change. 36 μL of 20% (w/v) APS solution was then added, followed by 48 mg of blowing agent of sodium bicarbonate immediately after. The mixture was vigorously stirred with a vortex generator at room temperature and polymerization was completed in a few minutes.

Testing flow rates. The flow rate was calculated based on the diameter of the water outlet tubing using the formula:

$$\text{Flow rate per gram} = 3.14 * (r)^2 (h)(t)^{-1} (m)^{-1} \quad (3-1)$$

In mL min^{-1} , where r =tube radius= 0.4 cm, h =height of water column in tube in cm, t =time in minutes, m =mass in grams.

Also, the required physiological flow rate²¹ is $0.05\text{-}0.15 \text{ mL} \cdot \text{min}^{-1} \cdot \text{g}^{-1}$, though this varies⁷⁵. Hence, according to the above equation, height of water column must be 0.4-1.2 cm for a SPH size of 4 g to mimic physiological flow rate. Flow rate was calculated by placing approximately 4 g of the SPH in the flow vessel and water was passed through the SPHs in the flow vessel using a peristaltic pump such that a uniform water column is obtained in the outlet tubing.

Design of the Flow Phantom System and Experimental Setup

The tumor phantom had to be fit into a flow vessel so that the blood-mimicking medium, i.e. water, could be passed through it at the physiological flow rate of blood in tumor tissue using the appropriate experimental setup. It was designed using AutoCAD[®] engineering design software and described in the Results section.

Specifications of the Experimental Setup. The experimental setup consisted of the following components: a radiofrequency induction heater, DC power supply, function generator, oscilloscope, recirculating water bath, temperature probes, a peristaltic pump and a PC system. Their functions were as follows:

1. The radiofrequency induction heater used was a magneTherm™ version 1.5 (NanoTherics Limited, UK) device that is used to heat the magnetic nanoparticles inside the tumor phantom by high- frequency induction through a 17-turn water-cooled, copper coil inside the device. The device housed a wide sample aperture (44 mm) tube inside the coil enclosure into which the tumor phantom can be fit. Fig. 3-1 shows the flow vessel inside the coil enclosure. The A200 capacitor used in the magneTherm™ had a 200 nF capacitance to achieve the desired frequency range for the 17-turn coil.
2. The function generator was a GW INSTEK SFG-2004 model used to generate a square waveform at a frequency of 110.8 kHz, which is the ideal operating frequency for the 17-turn coil.
3. The DC power supply was supplied by a digimess Concept series DC power supply SM5020 device. The operating voltage was set at 28.8 V, which induced a current of 11 mA.
4. An ISO-TECH ISR622 20 MHz oscilloscope was used to monitor the signal voltage passing through the coil.
5. A Julabo 250 recirculating water bath was used to continuously cool the coils to prevent the sample being exposed to the non-specific heating caused by the heat induction by the high-frequency magnetic fields in the coils. The water tubing used to connect the bath to the magneTherm™ had an internal diameter of 5 mm.
6. The peristaltic pump used to pump the blood-mimicking medium through the tumor phantom was a Cole-Parmer Masterflex 4S.
7. A Neoptix ReFlex Fiber Optic Temperature sensor was used with 2 temperature probes inserted into the tumor phantom to record the bulk rise in temperature due to the heating of the IONPs upon the application of the AC magnetic field through the coils. A PC system recorded the temperatures using Neoptix software.

The connections were made as shown in Fig.3-2.

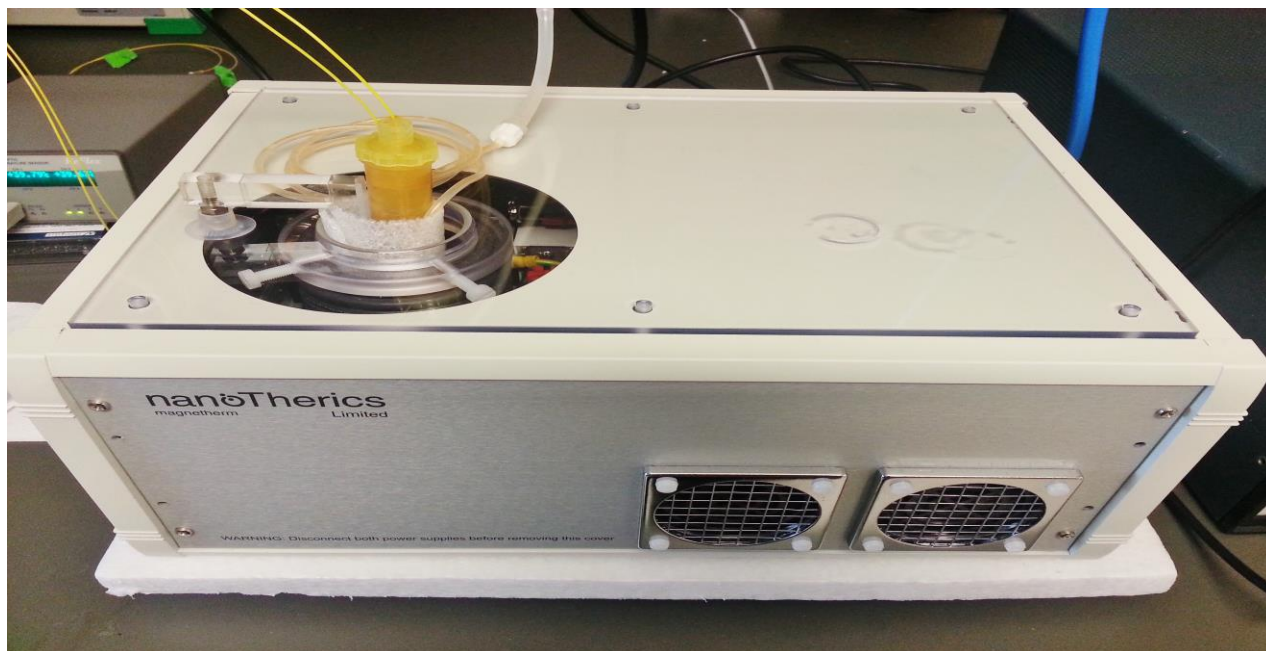


Figure 3-1. Position of the flow vessel inside the magneTherm™ chamber with the required auxiliary connections in place.



Figure 3-2. Experimental setup.

Characterization and Visualization of the IONPs

The Iron (III) oxide nanopowder used in this research study claimed to have IONPs of sizes less than 50 nm, as mentioned by the Sigma- Aldrich manufacturer. No information concerning the polydispersion of the nanoparticle size was given and hence DLS was used to determine the hydrodynamic size and polydispersity of this nanopowder. DLS or Photon correlation spectroscopy (PCS) is a technique used to obtain the size distribution profile of particles in suspension, in this case being IONPs in water. The diffusion coefficient of the nanoparticles in solution is determined to find the hydrodynamic radii of the spheres and the polydispersity of the colloidal solution. Zeta potential is another parameter that is a measure of the electrokinetic potential of the IONPs when suspended in water. It indicates the stability of the colloids, i.e. the IONPs in water. It is measured using the same DLS device.

A solution of 20 mg mL⁻¹ of the nanopowder in DI water was prepared and filtered twice through a 0.45 μm PVDF filter, to within the limits of DLS detection. DLS analysis was done using a Brookhaven ZetaPALS Particle Size Analyzer and Zeta Potential Analyzer used at a 90° scattering angle. The Zeta potential was measured at a current of 0.63 mA and electric field of 14.47 V cm⁻¹.

The samples were adequately prepared by thin slicing and freeze-drying. They were then carbon-coated overnight prior to SEM use. An FEI XL-40 FEG-SEM was used to capture high-resolution, high- magnification images for 3 purposes in this project: i) the shape and size of the IONPs, ii) the surface topography and size of channels in the SPHs produced, and iii) the visualization of the IONPs attached to the

surfaces of the SPHs. The SEM was operated at an accelerating voltage of 20 kV and at 162 μA for high resolution of the IONPs.

Quantification of Iron (III) Oxide in the SPHs

First, the SPHs containing the IO were prepared to create tumor phantoms containing the IONPs. Then, the amount of Iron (III) oxide (IO) taken up by the SPHs was quantified using the spectrophotometric method of Iron estimation. The concentrations were verified using Inductively coupled plasma mass spectrometry (ICP-MS).

Preparation of Tumor Phantom containing the IONPs

The required amount of IO was placed in deionized (DI) water in a glass beaker and the polymer was immersed in it to swell at equilibrium over a period of 3 days. 1.5 g of IO in 150 mL DI water (concentration of 10 mg mL^{-1}) was found to provide optimal IONP uptake by the swelling polymer at the end of 3 days. On the 3rd day, the SPH formed by the uptake of water and IONPs is taken out of the beaker and the surface dabbed with paper towels to remove excess IO and water from the outside. The weight and volume measurements of the IONP-containing SPHs (IONP-SPHs) are then taken using a weighing balance and a volumetric flask to determine the increase in weight and volume over 3 days. The amount of IO absorbed by the swollen SPH is quantified using the spectrophotometric method, which is described in the next sub-section.

Spectrophotometric Estimation of IO Content in the IONP-SPHs

Concentrated nitric acid, hydroxylamine hydrochloride, sodium acetate and 1,10-o-phenanthroline monohydrate were obtained from Sigma- Aldrich. Reagent A (56% hydroxylamine hydrochloride), Reagent B (10%) sodium acetate and Reagent C

(0.26%) 1,10- o-phenanthroline monohydrate were prepared for the spectrophotometric estimation of Iron oxide content in the samples.

Digestion with Nitric Acid. 10 mg IO was added first to 2 mL concentrated ultrapure trace metal grade nitric acid, to obtain the final concentration as 5 mg mL^{-1} . A small sample was taken from different parts of the IONP- SPH (total around 0.045 g) and homogenized using a blade. It was then added to 1 mL concentrated nitric acid in a glass culture tube. The standard and the sample are left to digest overnight at 101°C in a heating bath.

Preparation of standard dilutions. From the standard Iron solution of 5 mg mL^{-1} , Iron calibration solutions were obtained by water dilutions in 15 mL Corning tubes. This was done by pipetting the required volumes of standard Iron solutions into the given volumes of DI water to obtain different concentrations of IO: 5, 10, 30, 60, 90, 100 and $120 \mu\text{g/mL}$.

Preparation of sample solutions. 2 dilutions of the samples, 30X and 60X, were prepared on the assay plate along with their duplicates.

Assay reaction. $36 \mu\text{l}$ of DI water was added to each well. The Iron calibration solutions were placed in one well per solution (7 in total), and one well was used as a negative control containing no IO. The samples were placed in 4 wells per sample (2 for the dilution and 2 for their duplicates). $10 \mu\text{l}$ from each calibration solution/ sample dilution were added to each well accordingly. $10 \mu\text{l}$ of DI water was added in the negative control well. $30 \mu\text{l}$ of Reagent A, $49 \mu\text{l}$ of Reagent B and $75 \mu\text{l}$ of Reagent C were added to each well in order. The solutions in the wells were mixed well through

pipetting or using a horizontal shaker and the plate was incubated for 10 minutes at room temperature before the readings were taken.

Spectrophotometer readings. Absorbance (A) readings are taken using a spectrophotometer (Biotek Synergy HT Multi-Mode Microplate Reader) that takes A readings at 508 nm, which is the maximum absorbance for the Iron (II)- o-phenanthroline complex.

Preparation of calibration curve. A values of the calibration standards measured were plotted on the y axis as a function of the respective known analyte concentrations($C, \mu\text{g mL}^{-1}$) on the x axis using an Excel spreadsheet. Using the line equation, the C value of the unknown sample was calculated. Final concentration in the sample was determined using the formula:

$$C * \text{dilution factor} = \text{concentration of IO } (\mu\text{g IO/mL nitric acid}) \quad (3-2)$$

The average of the concentration values for each dilution was calculated to give the final concentration in unknown sample ($\mu\text{g IO/mL nitric acid}$).

Simulating MFH in IONP-SPHs under Varying Flow Conditions

Approximately 4 g of the IONP-SPH was packed into the flow vessel and final temperatures were recorded under three conditions:

1. SPH without water in the phantom
2. SPH with stationary water but no flow
3. SPH with water flow through the phantom.

Using a syringe pump, DI water was flushed through the vessel till all the excess IO attached to the SPH surface is washed away. The vessel was then stoppered and its lateral surface was covered with polyurethane foam. This foam acted as a thermo-

insulator to prevent heat loss and also to prevent non-specific heating from the heated coils in the magneTherm™ chamber. Two temperature probes were inserted into different positions (near the top and bottom) in the SPH. The insulated vessel was then placed atop a 61 mm spacer inside the magneTherm™ chamber. This was done so that the tumor phantom is located in the middle of the coils in the chamber, equidistant from the chamber walls. After allowing the temperature inside the vessel to equilibrate with the chamber temperature, the auxiliary equipment was switched on.

The frequency generator was set at 110.8 kHz frequency and at 50% load and the oscilloscope was set to display 20 V/division. After recording the temperature readings for 30 seconds, the field was turned on by slowly increasing the voltage to 29.9 V. Temperature readings were recorded for an hour and then the field was turned off. The temperature readings from both the probes were recorded and averaged.

For temperature measurements under flow, 5 mL water was added to the top of the tumor phantom. The pump was started at a flow rate of 0.08 mL min^{-1} at the same time the field was turned on. The negative pressure created by this flow rate enabled the water flow through the phantom at the required output flow rate of $0.05\text{-}0.15 \text{ mL min}^{-1} \cdot \text{g}^{-1}$.

CHAPTER 4 RESULTS AND DISCUSSION

Specifications and Design of the Flow Vessel

The flow vessel was required as a physical support for the tumor phantom under the flow conditions. This setup would be utilized to simulate hyperthermia in the tumor tissue under physiological blood flow.

During the early stages of this project different prototypes for the flow vessel were designed using AutoCAD[®] engineering design software. The final design is shown in Fig. 4-1. The dimensions were such that it would easily fit inside the coil enclosure chamber of the magneTherm[™]. The vessel was designed such that the tumor phantom would be in the center of the coils in the vertical axis, equidistant from the enclosure walls. The vessel had an outer diameter of 15 mm and the center of the vessel was 22 mm away from the walls. The coils started 20 mm below the top of the enclosure, and spanned 45 mm. The vessel was designed to accommodate openings for the two temperature probes and inlet and outlet tubing for the blood-mimicking medium.

The designed flow vessel had ideal specifications for the purposes of this project, but custom-building it proved to be time-consuming and expensive. Hence a more cost-effective, commercially available alternative was found, in the form of a Bio-Rad Econo-Column chromatography column (Fig. 4-2). The translucent column had a length of 50 mm and inner diameter of 15 mm, with a maximum volume of 9 mL and cross-sectional area of 1.77 cm², which fits the dimensions required for use with the magneTherm[™]. The porous polymer bed support at the bottom of the column would add to the support of the tumor phantom and prevent it from breaking apart during flow. A special brace

was fabricated to hold the flow vessel inside the chamber equidistant from the walls (Fig. 4-2).

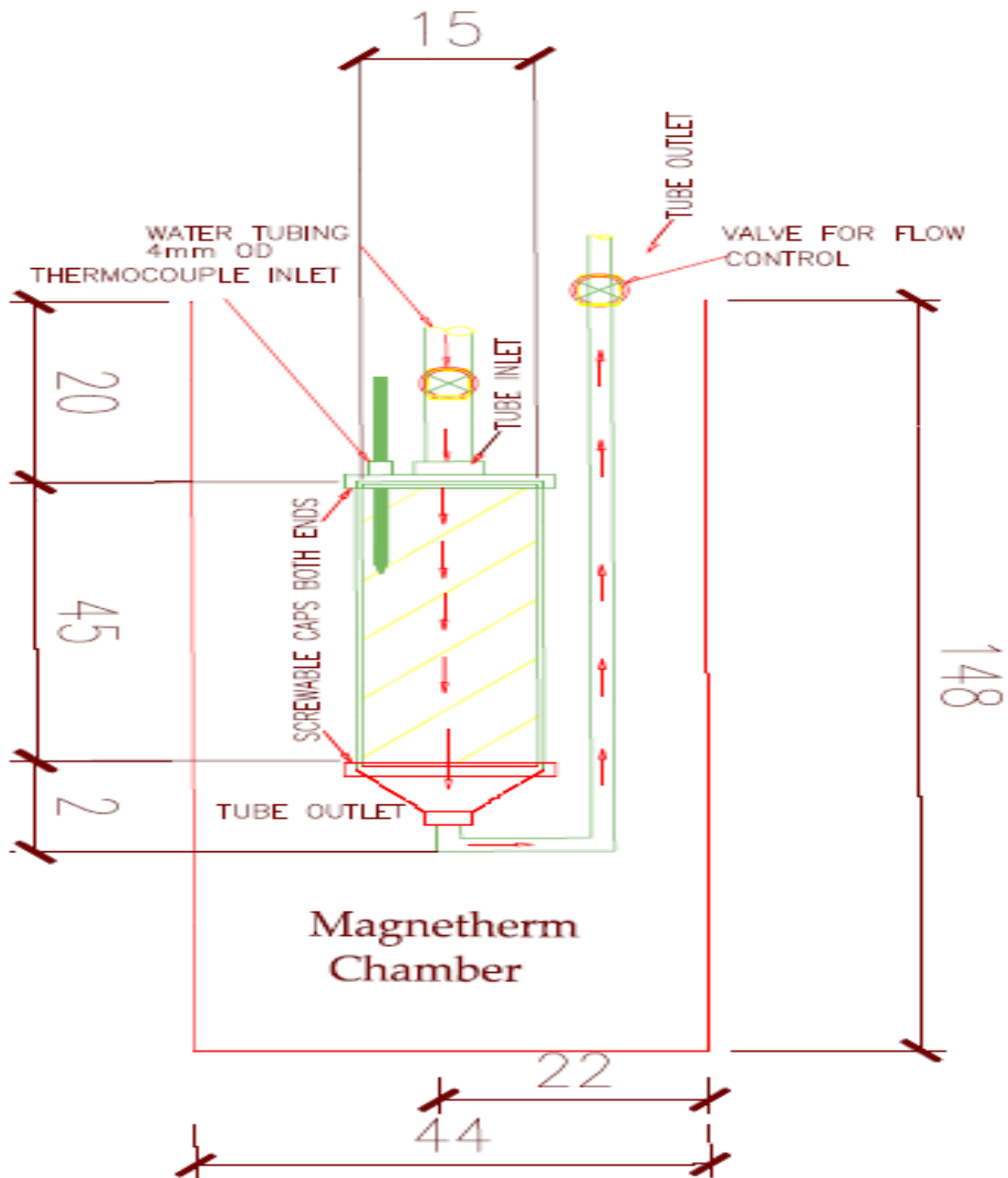


Figure 4-1. Schematic of the designed tumor flow phantom vessel. The vessel is shown with auxiliary inlet and outlet water tubing, as designed to fit in the magneTherm™ coil enclosure chamber (not to scale, all dimensions in mm).



Figure 4-2. The flow vessel with the tumor phantom, attached to a brace to hold it inside the magneTherm™ chamber.

Synthesis and Optimization of the SPHs

Rejection of Several Materials Tested as Tumor Phantoms

The most commonly used gel matrix for the creation of biomimetic phantoms is agarose. For encapsulation of particles, silica and Sephadex® are frequently utilized, as in chromatography and separation processes. These materials and their combinations were tested to see if they fulfilled the requirements as discussed in Chapter 3. They were rejected for the following reasons: a) The silica gel did not form a suitable gel matrix and instead formed a slurry with water, hence it did not mimic tissue structure; b) the agarose gel was not water-permeable and forming micro-channels in it for water flow would require their manual creation, which would be inefficient; c) high- and low-

melting point agarose gel mixtures in different ratios were tested. The purpose of this was to determine if controlled melting of the low melting-point agarose resulted in the creation of channels, but the melting was challenging and difficult to control; d) the silica-agarose gel mixture, Sephadex[®] G-10 and G-20 beads, Sephadex[®]-agarose gel mixture were among other gels tested but failed to satisfy the water permeability requirement, as shown in Table 4-1 (✓, ✗ refers to the material having or not having the property, respectively).

Table 4-1. Comparison of properties of candidates for tumor phantom.

Property	Agarose	Silica	Low MT-High MT agarose mix	Agarose-silica mix	Sephadex G-10 and G-20	P(AM-co-AA)/PEI IPN
Water permeability	✗	✓	✗	✗	✓	✓
Matrix	✓	✗	✓	✓	✗	✓
IONP loading	✓	✗	✓	✓	✗	✓
Thermal stability	✗	✓	✗	✗	✓	✓
Mechanical strength	✓	✗	✓	✓	✗	✓

Optimization of the AM/AA ratio of the Superporous hydrogels

Different AM/AA monomer concentration ratios of the SPHs were tested to determine the best AM/AA ratio that led to the phantom possessing the desired properties. The AM/AA ratios were chosen based on preliminary data published by Kim

et al.⁷⁴, for the properties of gelation kinetics, swelling behavior and mechanical strength.

For all AM/AA ratios, PEI was incorporated at 5% by weight, since the study⁷⁴ demonstrated that it takes only 2 minutes to reach equilibrium at this condition. This significantly decreased the water sorption rate compared to the other PEI weight % values. The initial AM/AA ratios tested were 0.8/0.2 AM/AA and 0.6/0.4 AM/AA as they had higher AM concentrations, hence higher swelling ratios. But they both proved to be too brittle to form a solid matrix due to their high swelling ratios.

Accordingly, the AM fraction was decreased and 0.2/0.8 AM/AA was tested. The SPHs were created by neutralizing the polymers so that polymers in solutions with pHs of 2.0, 3.0, 3.5, 4.0 and 5.0 were obtained and swelling carried out over 3 days (Fig. 4-3). The swelling ratios were found to be 1X, 1.5X, 8X, 20X and 25X respectively, as shown in Table 4-2. They were mechanically stable and did not lose structural integrity as easily as the 0.8/0.2 and 0.6/0.4 AM/AA ratios. Consequently, these SPHs were further tested for their water permeability.

The flow was controlled using the peristaltic pump, at an input flow rate of 0.08 mL min⁻¹. The flow rates through the SPHs were calculated using Equation 3-1. However, they were found to be higher than physiological flow rates and the 0.2/0.8 AM/AA ratio was eliminated from consideration as well.

By increasing the AM by a smaller amount, 0.4/0.6 and 0.5/0.5 AM/AA ratios were tested in the next step for the pH variations of 3.0, 4.5 and 5.0, as they were found to swell to a considerable extent without compromising mechanical stability. As shown in Table 4-3, both AM/AA ratios demonstrated flow rates within the physiological range.

At a pH of 5.0, 0.5/0.5 AM/AA and 0.4/0.6 AM/AA exhibited flow rates of 0.15 and 0.20 mL.min⁻¹.g⁻¹, respectively. Hence, both these SPH configurations, at PEI weight of 5%, were concluded to be suitable candidates for the tumor phantom. In later sections, they are tested for swelling and uptake of IONPs and for simulation of MFH in the designed flow system.

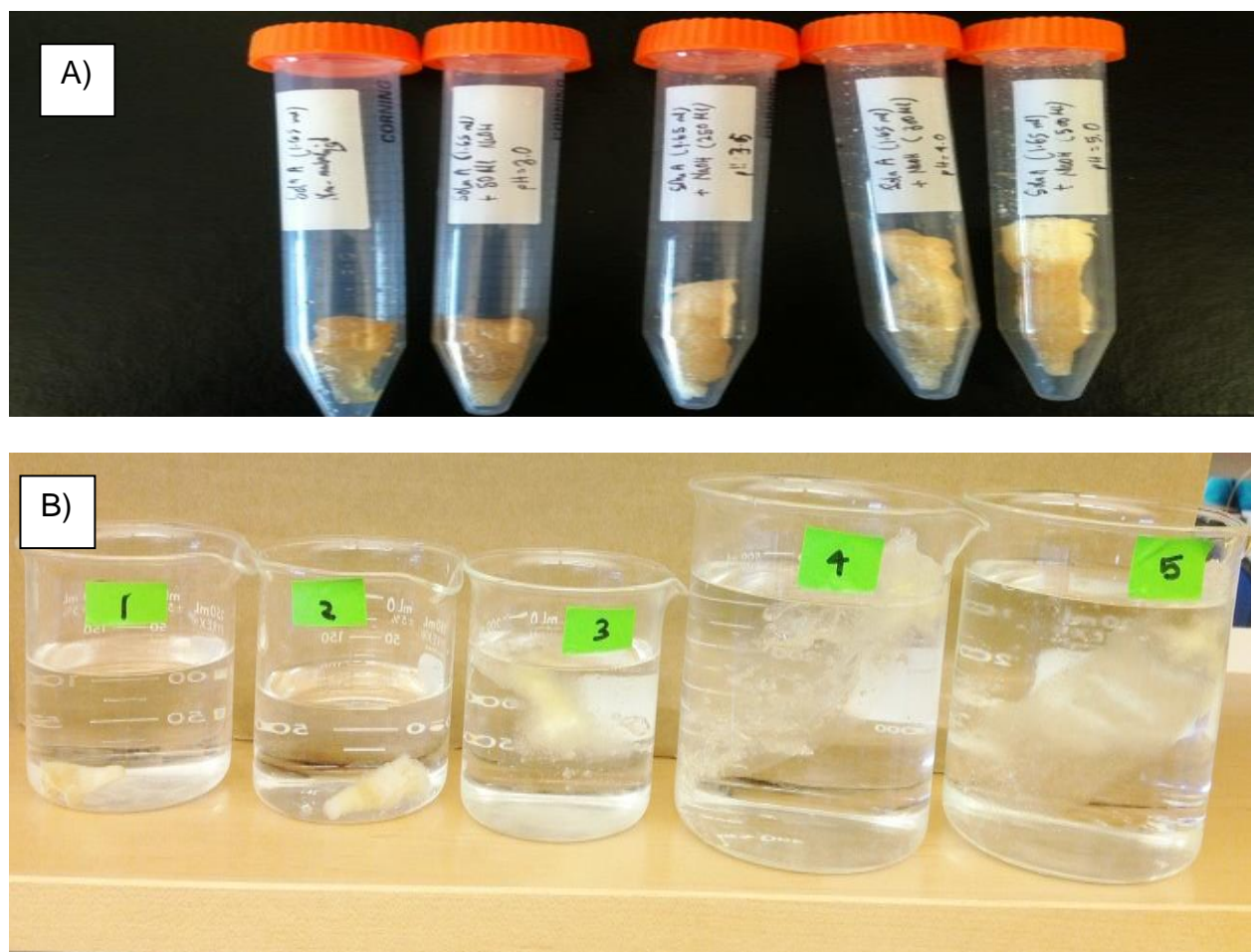


Figure 4-3. Swelling trend of 0.2/0.8 AM/AA polymers with increasing pH values. A) The neutralized polymers are at different pH values from L-R: 2.0, 3.0, 3.5, 4.0 and 5.0, respectively. B) The swollen SPHs after 3-day swelling.

Table 4-2. The swelling ratios of the 0.2/0.8 AM/AA SPHs after the 3-day swelling period.

pH	2.0	3.0	3.5	4.0	5.0
Volume (fold)	1X	1.5X	8X	20X	25X

Table 4-3. Flow rates in 0.5/0.5 AM/AA and 0.4/0.6 AM/AA SPHs (Pump flow rate=0.08 mL min⁻¹):

AM/AA	pH	Initial weight (g)	Final weight (g)	Flow rate (mL.min ⁻¹ .g ⁻¹)
a) 0.5/0.5	3.0	1.00	12.20	0.00
	4.5	1.10	15.00	0.01
	5.0	1.00	17.63	0.15
b) 0.4/0.6	3.0	1.00	5.44	0.00
	4.5	1.00	9.92	0.02
	5.0	1.10	27.86	0.20

Characterization and Visualization of the IONPs

DLS measurements of the uncoated Iron (III) oxide nanoparticles show a particle mean diameter of 61.3 nm, after suspension in water and filtering using a 0.45 µm PVDF filter to filter out the aggregates. Zeta potential was found to be 33.81 ± 1.63 mV, indicating moderate stability in aqueous suspension.

IONP sizes were also observed using SEM. The IONPs were dispersed on a carbon strip and observed using high-resolution, high- magnification images. Fig.4-4A shows a single spherical particle of diameter around 100 nm. Fig. 4-4B shows agglomerations of IONPs of similar, nearly consistent sizes. They agglomerate as they are uncoated.

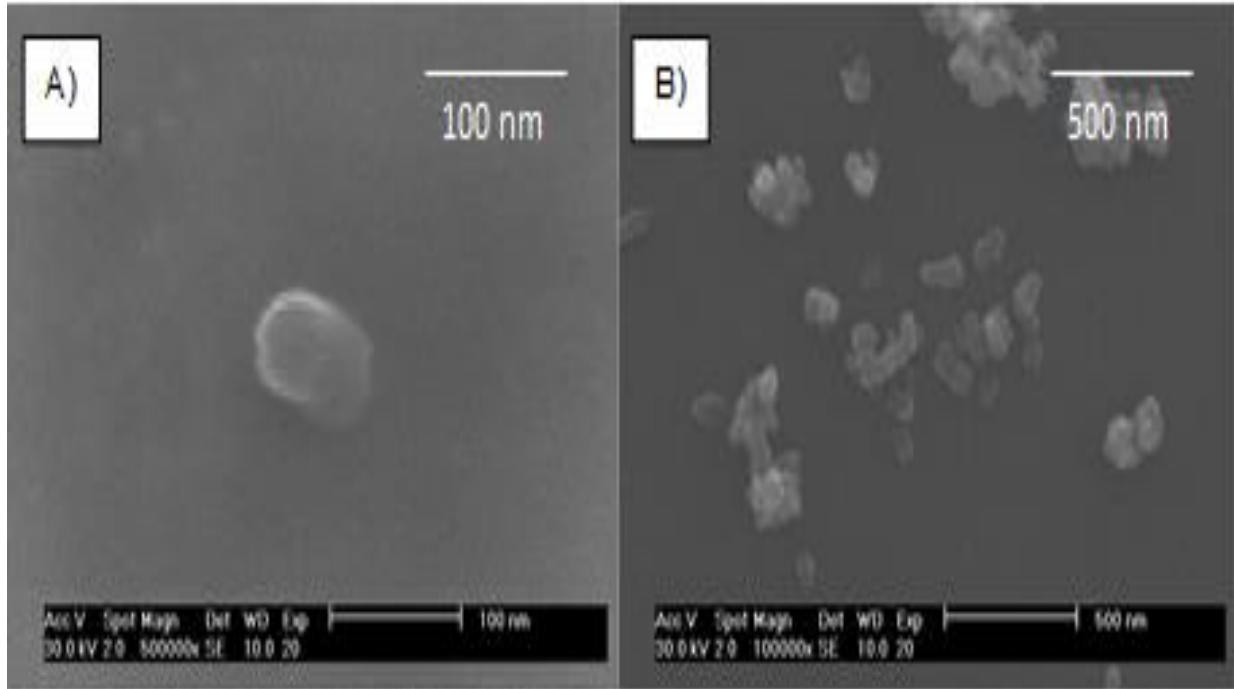


Figure 4-4. SEM images of the IONPs. A) A single nanoparticle of size around 100 nm at 500000X magnification, B) Scattered IONPs showing similar sizes, below 100 nm, at 100000X magnification.

Development of a Novel Method of Entrapment of the IONPs into the SPHs

The IONPs had to be entrapped or somehow bound to the SPH matrix to simulate the targeted binding of the IONPs to cancer cells in the body and enable their homogeneous distribution throughout the body of the SPH. Three methods were used to facilitate this property (Fig.4-5):

1. IONPs added before polymerization and before swelling
2. IONPs added after polymerization and after swelling
3. IONPs added after polymerization and during swelling

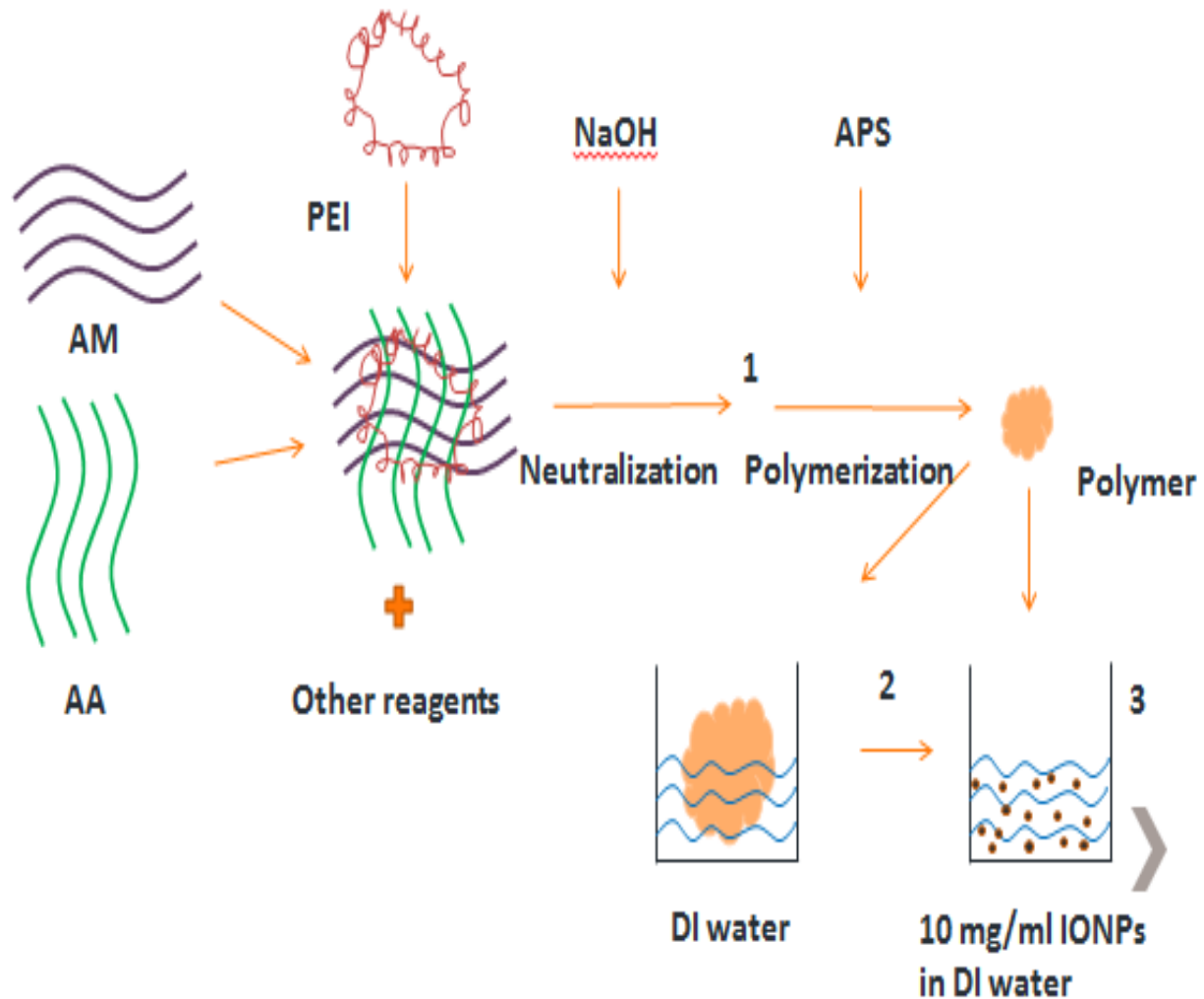


Figure 4-5. Development of a Novel Method of Entrapment of the IONPs into the SPHs. 1) IONPs added before polymerization and before swelling, 2) IONPs added after polymerization and after swelling, 3) IONPs added after polymerization and during swelling

In the first method, the IONPs were added to the stock solution just before polymerization. The IO concentrations achieved through this method were extremely low: the highest concentration of IO achievable through this method was only 4 mg/g SPH. This was because the amount of IO that could be placed in the 1 mL polymer stock solution before swelling had a limit of approximately 50 mg. Consequently this method, put restrictions on the concentration of IO in the final SPH, as only a limited

amount of IO could be added to the small volume (1 mL) of the stock solution. So it was concluded that this method was not viable.

The second method involved the SPH being added to a solution of 1.5 g IO in 150 mL water after it had reached swelling equilibrium. This method, however, enabled only weak surface binding of the IONPs to the SPH, hence it was not adequate.

The third method involved the addition of the polymer at the starting point of the swelling process to a solution of 1.5 g IO in 150 mL water. Under constant stirring and over a 3-day swelling period the gel reached a swelling equilibrium and resulted in the entrapment of large amounts of IO.

The IONP uptake and practicality of the three methods for our final goal were compared using the final temperatures (Fig.4-6) and concentrations (Fig.4-7) of the SPHs under one hour of applied AMF. The graph compared the final heating temperatures of the SPHs before and after washing, for each of the three methods (Note: $n=1$ in Fig. 4-6, 4-7 and 4-8 as these were preliminary measurements. The heating temperatures and concentrations were tested at later stages when the AM/AA ratio was finalized, for $n=5$).

The ability of the gel to retain the IONPs was proved to be significant only in the third method. This method demonstrated similar final temperature rises in the SPH before and after wash, concluding that the bulk of the IONPs are within the SPH matrix and do not escape the matrix during the washing step. Hence, this method was chosen as the most suitable for the purpose of this study. The major advantages of this method of IONP loading are: a) the easy tailoring of the amount of IO in the SPH by changing

the IO concentration in the solution and/or the period of swelling of the SPH, and b) easy manipulation of the swelling of the SPH by changing the AM/AA ratio and/or pH.

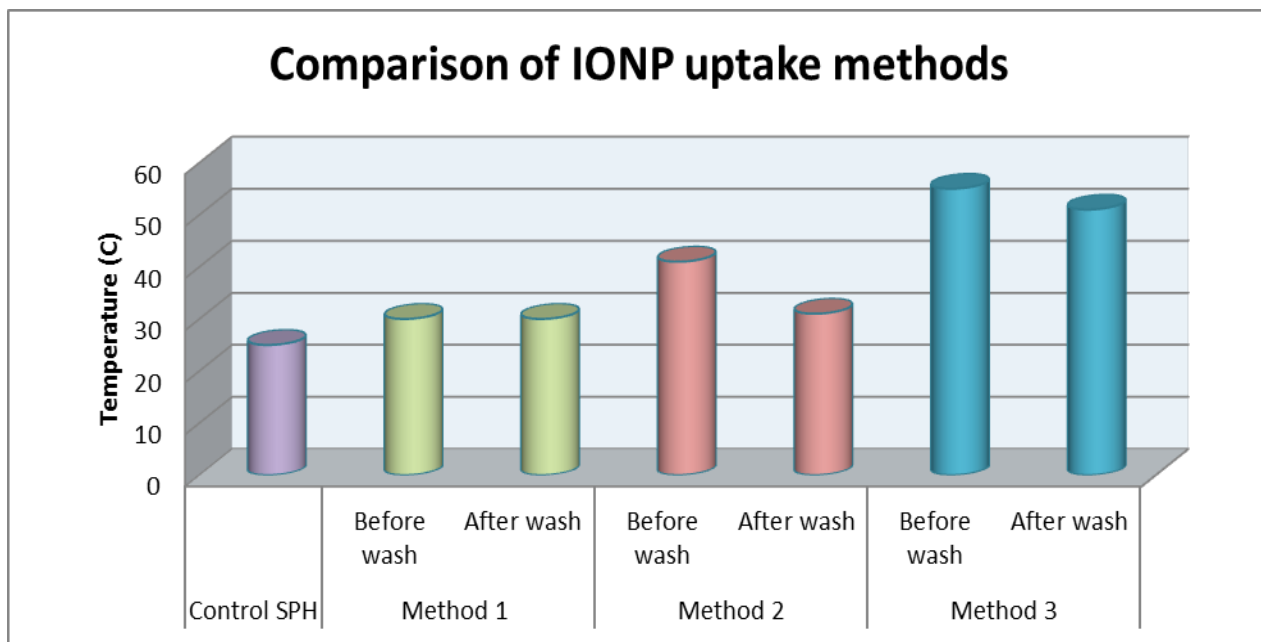


Figure 4-6. Comparison of IONP uptake methods using the final temperature attained by the SPHs in 1 hour ($H = 15.3 \text{ kA m}^{-1}$, $f = 110.8 \text{ kHz}$, $n=1$).

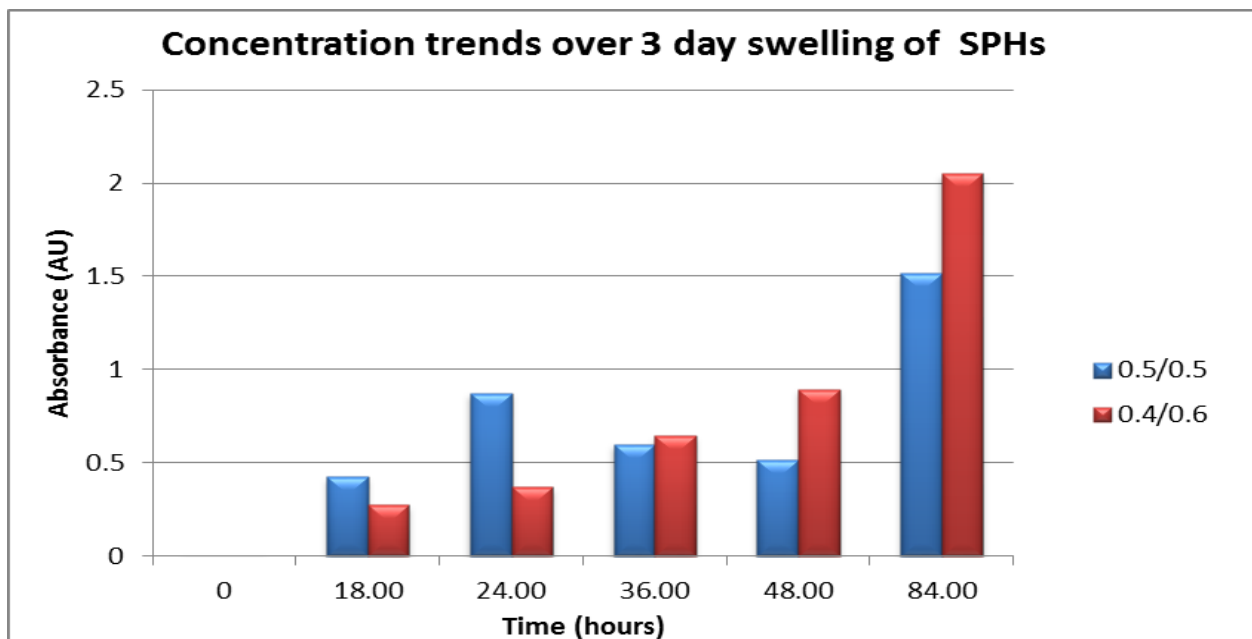


Figure 4-7. Concentration trends of the 0.5/0.5 and 0.4/0.6 AM/AA IONP-SPHs over the 3 day-swelling period ($n=1$)

Optimization of 0.4/0.6 AM/AA Polymer as the Tumor Phantom

Based on previous experiments, 0.4/0.6 and 0.5/0.5 AM/AA showed effective flow rates. As concluded in the previous section, the third method of IONP loading was shown to be optimal, as a result, it was tested for both the ratios. The final temperature for each ratio was tested on the 1st day and 3rd day after swelling in 1.5 g IO in 150 mL water (10 mg mL⁻¹ concentration). The 1st day temperatures were recorded as 36.45 and 29.4 °C for 0.5/0.5 and 0.4/0.6 AM/AA, respectively. The 3rd day temperatures were recorded as 46.55°C and 42.30°C (n=1) for 0.5/0.5 and 0.4/0.6 AM/AA, respectively, as shown in Fig.4-8. The final temperatures attained by either ratio were shown to be similar. The comparison between the control SPHs with no particles and the IONP-SPHs showed a slight increase in the swelling of the IONP-SPHs and the two different AM/AA ratios swell to the same degree, as shown in Fig.4-9. Based on these results, both ratios showed similar characteristics. From this point on, the experiments were standardized using 0.4/0.6 AM/AA exclusively as the tumor phantom.

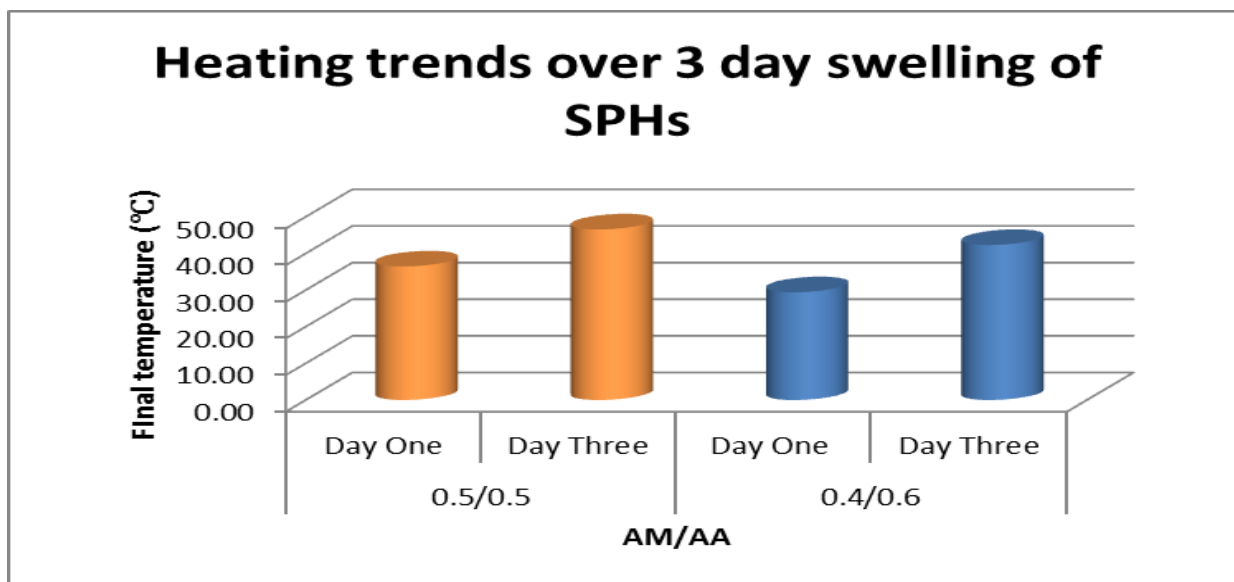


Figure 4-8. Heating trends of the 0.5/0.5 and 0.4/0.6 IONP-SPHs (n=1) over the 3 day-swelling period ($H = 15.3 \text{ kA m}^{-1}$, $f = 110.8 \text{ kHz}$).

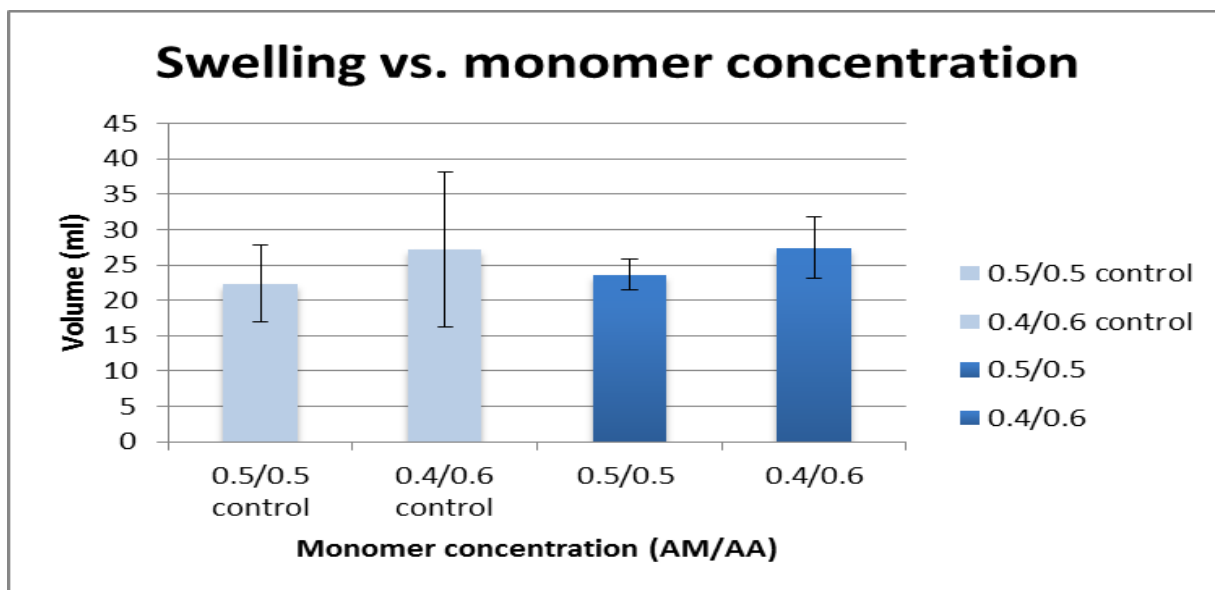


Figure 4-9. Comparison of the swelling of the 0.5/0.5 and 0.4/0.6 AM/AA control SPHs and IONP-SPHs (n=5) after the 3-day swelling period (n=5)

Quantification of the IONP Concentration in the 0.4/0.6 SPHs

Two different methods were applied in order to quantify the amount of IO in the IONP-SPHs. The first used chemical reaction of Iron with a reagent to generate colorimetric results. The detection limits of this method were appropriate for the expected IO concentration values. The second method, ICP-MS, was based on the spectral properties of Iron in its reduced state. It helped validate the colorimetric results and eliminate errors based on gel interference during the colorimetric assay. Both methods generated similar values when compared. The concentration of the IO in the 0.4/0.6 AM/AA IONP-SPHs was shown to be 16.42 ± 4.2 mg/ g IONP-SPH (n=5). These were heated up to hyperthermic temperatures and the final temperatures were recorded, as elucidated in the final section.

Visualization of the Superporous Hydrogels and IONP-Superporous Hydrogels

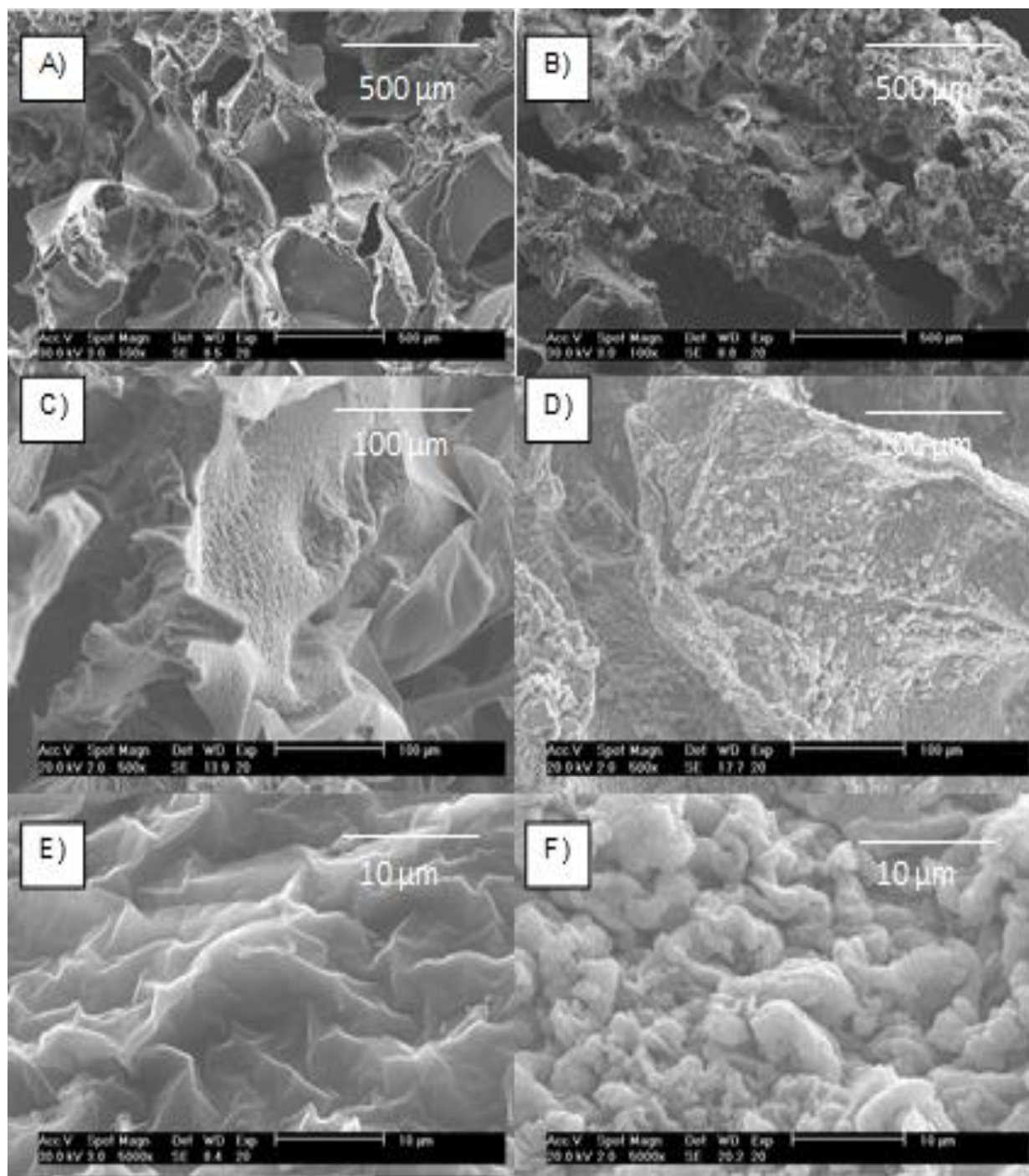


Figure 4-10. SEM images of the 0.4/0.6 SPHs at various magnifications. A) Surface of control SPH at 100X magnification showing channels through the SPH, B) Surface of IONP-SPH at 100X magnification, C) Surface of control SPH at 500X magnification, D) Surface of IONP-SPH at 500X magnification, E) Surface of control SPH 5000X magnification and F) Surface of IONP-SPH at 5000X magnification.

The surface topography of the 0.4/0.6 AM/AA freeze-dried SPHs with and without IONPs is shown in Fig.4-10. They show channels of varying sizes through the SPHs that enable flow of the blood-mimicking medium. Also, the surfaces of the IONP-SPHs (SPHs having entrapped IONPs) that are visualized in Figs. 4-10B, D and F show rough surfaces as compared to the control SPHs. This is possibly attributed to the IONPs being electrostatically- bound to the surface of the SPH as the IONPs are positively charged, whereas the SPHs are negatively charged, hence non-specific binding occurs. The rough surfaces also could indicate the presence of IONPs under the surface of the SPHs, which are taken up during swelling and consequently entrapped in the body of the SPHs.

Heating curves of IONPs under Varying Flow Conditions

Final temperatures of the IONP-SPHs under an applied AMF were recorded for an hour under different conditions of flow, to determine the bulk temperature rise in the tumor phantom. This was performed for the purposes of testing the cooling effect of the flowing blood-mimicking medium on magnetic fluid hyperthermia. It has been shown earlier¹³ that targeted intracellular hyperthermia, even without a perceptible bulk temperature rise, can be effective in treating small tumors and metastatic cancers. Nevertheless, the main goal of this study was to test the hypothesis that cooling blood flow has little effect on the MFH in tissue. This required bulk heating of the tumor phantom by elevating it to required hyperthermic temperatures under the applied AMF.

For experimental purposes, DI water was used as the blood-mimicking medium initially. Later, 15% saline solution was tested as the medium as it has similar specific heat capacity to blood. Approximately 4 g of the SPH was inserted into the flow vessel and final temperatures were recorded under three conditions:

1. SPH without water in the phantom
2. SPH with stationary water but no flow
3. SPH with water flow through the phantom.

These three conditions were tested over a period of 1 hour and field conditions of $H = 15.3 \text{ kA m}^{-1}$ and $f = 110.8 \text{ kHz}$. Under the first condition, the final temperature attained was $51.71 \pm 1.28^\circ\text{C}$, the second, $52.68 \pm 0.97^\circ\text{C}$, and the third, $51.17 \pm 3.56^\circ\text{C}$ ($n=5$) (Fig. 4-11). The final temperatures obtained in each case were similar, showing that the flowing water has no measurable effect on the final temperatures under the heating conditions simulated.

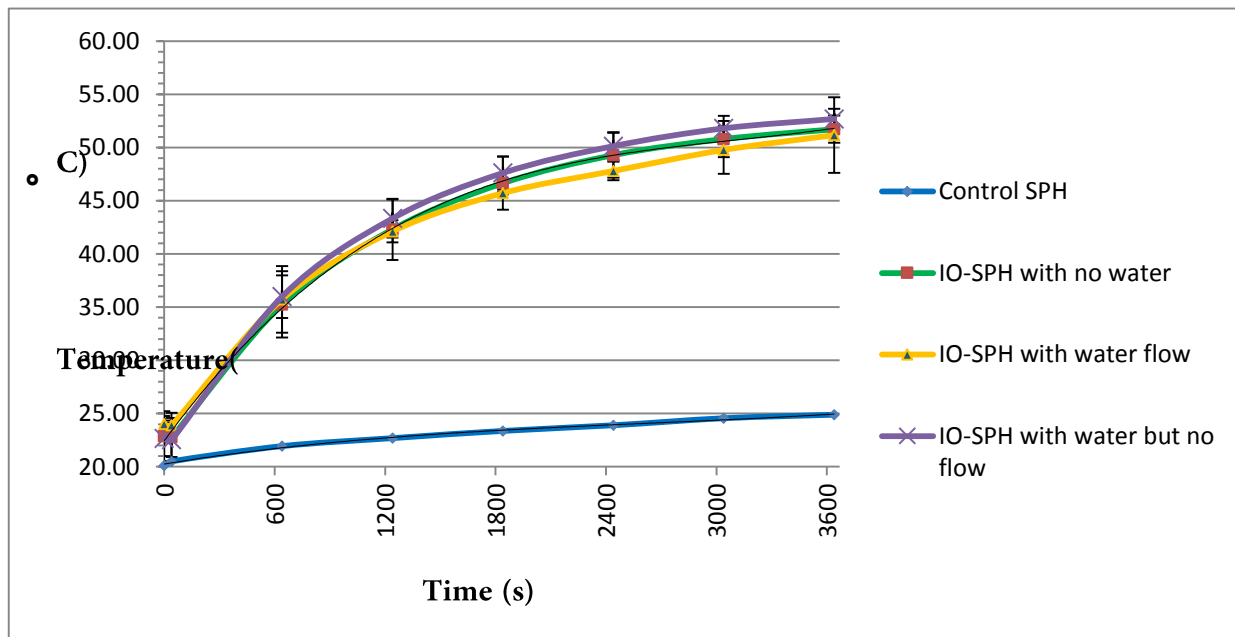


Figure 4-11. Heating trends of 0.4/0.6 AM/AA IONP-SPHs ($n=5$) under varying water flow conditions ($H = 15.3 \text{ kA m}^{-1}$, $f = 110.8 \text{ kHz}$).

Challenges encountered while Simulating Physiological Conditions

Physiological Temperature

To mimic physiological temperature in the tumor phantom, the flow vessel containing the tumor phantom was required to be maintained at a constant temperature

of 37°C. Due to the technical constraints of the operating temperature range of the magneTherm™ and the difficulty of enclosing the whole flow system in an incubator, it was not practical. In order to overcome this problem, the flow vessel containing the tumor phantom was pre-heated up to 40°C in an incubator-shaker device. It was then placed in the magneTherm™ and the field turned on when the temperature dropped to 37°C. The temperature readings showed that not much of a difference (2-5°C) is seen among the final temperatures obtained (Table 4-4). It is plausible that the final temperature obtained was independent of the initial temperature. If this were true, under ideal conditions of a constant 37°C may register higher temperatures as the heating losses to the environment would be lessened considerably. However, these results were inconclusive due to the fact that the system was not at steady state and suffered heat losses to the environment.

Table 4-4. Temperature (T) readings of the IONP-SPHs at different initial temperatures ($H = 15.3 \text{ kA m}^{-1}$, $f = 110.8 \text{ kHz}$, $n=1$).

T at 0s (°C)	T at 1800s (°C)	T at 3600s (°C)
20.00	37.32	42.96
35.00	43.74	47.08
37.00	41.26	44.84

Blood-Mimicking Medium

To move towards more physiological conditions, we substituted DI water for a blood-mimicking medium, 15% saline solution. It was selected based on its thermal conductivity k of $0.510 \text{ Wm}^{-1}\text{K}^{-1}$, which is nearly equal to that of whole human blood, whose k is $0.506 \text{ Wm}^{-1}\text{K}^{-1}$. However, when it was flowed through the IONP- SPH, it

caused shrinkage in the SPH to about a third of its original volume (Fig.4-12). This could be attributed to the osmotic effect of the higher salt concentration in the saline solution.

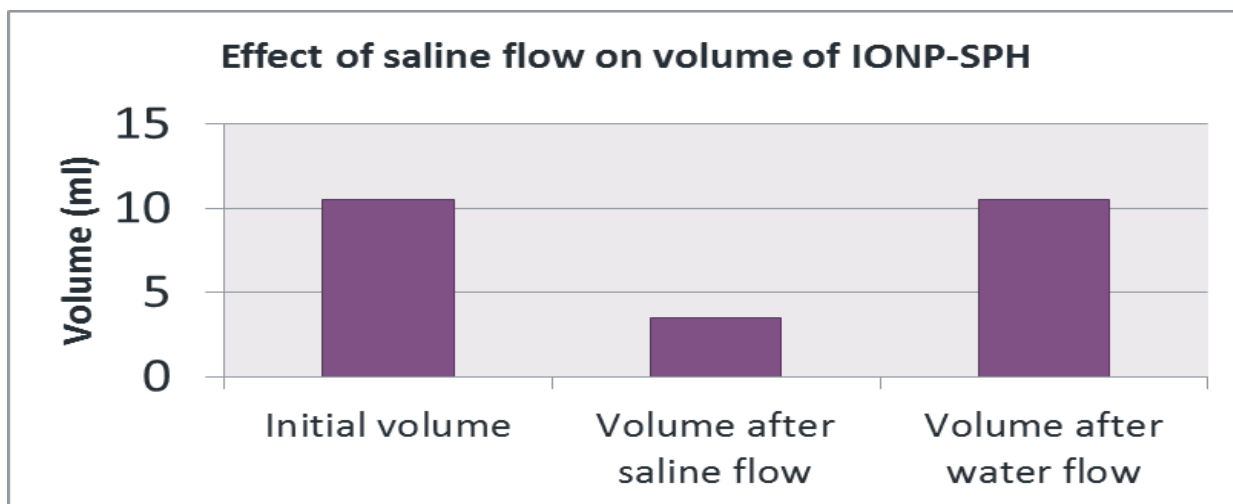


Figure 4-12. Effect of saline flow on volume of IONP-SPH

Based upon our observations, the saline flow through the IONP-SPH resulted in an increase in IONP concentration proportional to the decrease in volume of the IONP-SPH. This phenomenon could be used to enhance the concentration of the IONPs in the SPHs, but this theory will have to be tested under more rigorous conditions.

CHAPTER 5 CONCLUSIONS

In this research project, the overall goal of developing and testing a novel blood perfusion flow phantom system to study the heating effects of MFH *in vitro* was accomplished. The following objectives supported the main goal: design of the flow system, selection of polymer as tumor phantom and development of a novel IONP-loading technique.

Using AutoCAD[®], we designed a reliable perfused flow device for MFH studies. We incorporated the structural specifications (dimensions, tubing, etc.) for flow perfusion. A previously reported polymer of P(AM-co-AA)/PEI was optimized for 0.4/0.6 AM/AA monomer weight ratio and selected as the tumor phantom. The swollen SPHs were shown under SEM imaging, to have continuous pores between 100-1000 μm diameter that mimic tumor microvasculature. Subsequently, the first objective was accomplished: design and development of a flow device and a novel tumor phantom.

After experimenting with different methods of IONP loading in the SPHs, a novel technique for IONP entrapment was created. This method demonstrated that around high amounts of the IONPs can be entrapped in the body of the SPH, and do not escape during water flow. Tailoring the initial concentration of IO in the solution could potentially lead to corresponding changes in uptake by the SPH. This method was demonstrated to be efficient in the manipulation of the final IONP concentration in the SPH via the modification of the initial concentration of the IONP solution and the period of swelling. Average IONP concentration of 16.42 ± 4.2 mg/ g IONP-SPH was achieved over a 3-day swelling period, as validated by spectrophotometric estimation and ICP-

MS. Therefore, the second objective of the study, to enable controllable IONP loading at required concentrations in the tumor phantom, was achieved.

The IONP-SPH was placed in the designed flow vessel, which enabled its efficient immobilization during the desired flow conditions. Physiologically relevant flow rates ($0.05\text{-}0.15\text{ mL}\cdot\text{min}^{-1}\cdot\text{g}^{-1}$ tumor) were achieved by modifying the pump pressure. Under the applied field and flow conditions, the IONP-SPH in the flow phantom was able to reach hyperthermic temperatures of up to $51.71 \pm 1.28^\circ\text{C}$. Under the condition of no water in the SPH, the IONP-SPH also reached final temperatures of $52.68 \pm 0.97^\circ\text{C}$ as opposed to $51.17 \pm 3.56^\circ\text{C}$ under the stationary water (no flow) conditions.

A major caveat to this study is that, as the focus was mainly on the design and development of the tumor phantom, testing of MFH was only carried out at one flow rate of $0.2\text{ mL}\cdot\text{min}^{-1}\cdot\text{g}^{-1}$. Further testing at different flow rates is needed to determine whether this is a truly relevant model. According to preliminary calculations (*C. Rinaldi, personal communication*), there should be a measurable effect on heating in the SPHs due to their high porosity upon swelling. A possible reason this may not have been observed is due to channeling of the water through the SPH (channeling occurs when the liquid flow through the large void spaces). Therefore, the bulk of the water flow through the channels may not have been near enough to the temperature probes for these effects of high flow rate on heat transport to be measured.

This study therefore proved successful in the creation of a relatively easy to use, thermal blood perfusion flow phantom to study the heating effects of MFH *in vitro*. The phantom system developed appears promising as a model system in future MFH studies for tumor therapy.

CHAPTER 6 FUTURE DIRECTIONS

An incubator system large enough to accommodate the magneTherm™, together with the tumor phantom in the flow vessel, could be used to maintain the whole system at the required physiological temperature of 37°C. This could overcome the technical difficulty of not having the system incubated during MFH simulation.

Also, a better blood-mimicking medium with similar thermal properties to blood would be useful to simulate blood flow in the phantom.

The physical properties of the hydrogel like specific heat, conductivity, mass density etc. should be taken into consideration as they differ from human tissue. These studies suggest that the existing theories for heat mechanisms could be used to further extend this model, both theoretically and experimentally, for temperature distribution analysis, primarily keeping in mind blood perfusion characteristics.

LIST OF REFERENCES

1. Moroz P, Jones SK, Gray BN. Magnetically mediated hyperthermia: current status and future directions. *Int J Hyperthermia*. 2002;18:267-284.
2. Feldmann HJ, Molls M, Vaupel P. Blood flow and oxygenation status of human tumors. Clinical investigations. *Strahlenther Onkol*. 1999;175:1-9.
3. Lin C-T, Liu K-C. Estimation for the heating effect of magnetic nanoparticles in perfused tissues. *International Communications in Heat and Mass Transfer*. 2009;36:241-244.
4. Suto M, Kosukegawa H, Maruta K, Ohta M, Tohji K, Jeyadevan B. Heat diffusion characteristics of magnetite nanoparticles dispersed hydro-gel in alternating magnetic field. *Journal of Magnetism and Magnetic Materials*. 2009;321:3483-3487.
5. Hergt R, Andra W, d'Ambly CG, et al. Physical limits of hyperthermia using magnetite fine particles. *Magnetics, IEEE Transactions on*. 1998;34:3745-3754.
6. Giordano MA, Gutierrez G, Rinaldi C. Fundamental solutions to the bioheat equation and their application to magnetic fluid hyperthermia. *Int J Hyperthermia*. 2010;26:475-484.
7. Bagaria HG, Johnson DT. Transient solution to the bioheat equation and optimization for magnetic fluid hyperthermia treatment. *Int J Hyperthermia*. 2005;21:57-75.
8. Pankhurst QA, Thanh NTK, Jones SK, Dobson J. Progress in applications of magnetic nanoparticles in biomedicine. *Journal of Physics D: Applied Physics*. 2009;42:224001.
9. Jurgons R, Seliger C, Hilpert A, Trahms L, Odenbach S, Alexiou C. Drug loaded magnetic nanoparticles for cancer therapy. *Journal of Physics: Condensed Matter*. 2006;18:S2893.
10. Scherer F, Anton M, Schillinger U, et al. Magnetofection: enhancing and targeting gene delivery by magnetic force in vitro and in vivo. *Gene Ther*. 2002;9:102-109.
11. Plank C, Schillinger U, Scherer F, et al. The magnetofection method: using magnetic force to enhance gene delivery. *Biol Chem*. 2003;384:737-747.
12. Dobson J. Remote control of cellular behaviour with magnetic nanoparticles. *Nat Nanotechnol*. 2008;3:139-143.
13. Creixell M, Bohórquez AC, Torres-Lugo M, Rinaldi C. EGFR-targeted magnetic nanoparticle heaters kill cancer cells without a perceptible temperature rise. *ACS nano*. 2011;5:7124-7129.

14. Wang N, Ingber DE. Probing transmembrane mechanical coupling and cytomechanics using magnetic twisting cytometry. *Biochem Cell Biol.* 1995;73:327-335.
15. Hughes S, El Haj AJ, Dobson J. Magnetic micro- and nanoparticle mediated activation of mechanosensitive ion channels. *Med Eng Phys.* 2005;27:754-762.
16. Mannix RJ, Kumar S, Cassiola F, et al. Nanomagnetic actuation of receptor-mediated signal transduction. *Nat Nanotechnol.* 2008;3:36-40.
17. Berry CC. Possible exploitation of magnetic nanoparticle–cell interaction for biomedical applications. *J Mater Chem.* 2005;15:543-547.
18. Cho HS, Dong Z, Pauletti GM, et al. Fluorescent, superparamagnetic nanospheres for drug storage, targeting, and imaging: a multifunctional nanocarrier system for cancer diagnosis and treatment. *ACS Nano.* 2010;4:5398-5404.
19. Fahlvik AK, Klaveness J, Stark DD. Iron oxides as MR imaging contrast agents. *J Magn Reson Imaging.* 1993;3:187-194.
20. Bowen CV, Zhang X, Saab G, Gareau PJ, Rutt BK. Application of the static dephasing regime theory to superparamagnetic iron-oxide loaded cells. *Magn Reson Med.* 2002;48:52-61.
21. Krishnan KM. Biomedical Nanomagnetism: A Spin Through Possibilities in Imaging, Diagnostics, and Therapy. *IEEE Trans Magn.* 2010;46:2523-2558.
22. Gleich B, Weizenecker J. Tomographic imaging using the nonlinear response of magnetic particles. *Nature.* 2005;435:1214-1217.
23. Weizenecker J, Gleich B, Rahmer J, Dahnke H, Borgert J. Three-dimensional real-time in vivo magnetic particle imaging. *Phys Med Biol.* 2009;54:L1-L10.
24. Goodwill PW, Scott GC, Stang PP, Conolly SM. Narrowband magnetic particle imaging. *IEEE Trans Med Imaging.* 2009;28:1231-1237.
25. Johannsen M, Gneveckow U, Eckelt L, et al. Clinical hyperthermia of prostate cancer using magnetic nanoparticles: presentation of a new interstitial technique. *Int J Hyperthermia.* 2005;21:637-647.
26. Jordan A, Scholz R, Wust P, et al. Effects of magnetic fluid hyperthermia (MFH) on C3H mammary carcinoma in vivo. *Int J Hyperthermia.* 1997;13:587-605.
27. Lu AH, Salabas EeL, Schüth F. Magnetic nanoparticles: synthesis, protection, functionalization, and application. *Angewandte Chemie International Edition.* 2007;46:1222-1244.

28. Berry CC, Curtis ASG. Functionalisation of magnetic nanoparticles for applications in biomedicine. *Journal of physics D: Applied physics*. 2003;36:R198.
29. Pankhurst QA, Connolly J, Jones SK, Dobson J. Applications of magnetic nanoparticles in biomedicine. *Journal of physics D: Applied physics*. 2003;36:R167.
30. Whittaker ET. History of the Theories of Ether and Electricity from the Age of Descartes to the Close of the Nineteenth Century. London and Dublin: Longmans, Green and Co.; 1910.
31. Schenck JF. The role of magnetic susceptibility in magnetic resonance imaging: MRI magnetic compatibility of the first and second kinds. *Medical physics*. 1996;23:815.
32. Thorek DL, Chen AK, Czupryna J, Tsourkas A. Superparamagnetic iron oxide nanoparticle probes for molecular imaging. *Ann Biomed Eng*. 2006;34:23-38.
33. Kurti N. Selected Works of Louis Néel. New York: Gordon and Breach; 1988:407-427.
34. Rosensweig RE. Heating magnetic fluid with alternating magnetic field. *Journal of Magnetism and Magnetic Materials*. 2002;252:370-374.
35. Brown Jr WF. Thermal fluctuations of a single-domain particle. *Physical Review*. 1963;130:1677.
36. Gonzales-Weimuller M, Zeisberger M, Krishnan KM. Size-dependant heating rates of iron oxide nanoparticles for magnetic fluid hyperthermia. *Journal of Magnetism and Magnetic Materials*. 2009;321:1947-1950.
37. Ortega D, Pankhurst QA. Magnetic hyperthermia. in: O'Brien P, (ed). Nanoscience. Vol 1. Cambridge: Royal Society of Chemistry; 2013:66.
38. Tavill AS, Bacon BR. Hemochromatosis: how much iron is too much? *Hepatology*. 1986;6:142-145.
39. Allémann E, Leroux JC, Gurny R, Doelker E. In vitro extended-release properties of drug-loaded poly(DL-lactic acid) nanoparticles produced by a salting-out procedure. *Pharm Res*. 1993;10:1732-1737.
40. Gref R, Minamitake Y, Peracchia MT, Trubetskoy V, Torchilin V, Langer R. Biodegradable long-circulating polymeric nanospheres. *Science*. 1994;263:1600-1603.
41. Curtis AS, Varde M. Control of cell behavior: topological factors. *J Natl Cancer Inst*. 1964;33:15-26.

42. Gupta AK, Gupta M. Synthesis and surface engineering of iron oxide nanoparticles for biomedical applications. *Biomaterials*. 2005;26:3995-4021.
43. CF Chan D, B Kirpotin D, A Bunn P. Synthesis and evaluation of colloidal magnetic iron oxides for the site-specific radiofrequency-induced hyperthermia of cancer. *Journal of Magnetism and Magnetic Materials*. 1993;122:374-378.
44. Briley-Saebo K, Bjørnerud A, Grant D, Ahlstrom H, Berg T, Kindberg GM. Hepatic cellular distribution and degradation of iron oxide nanoparticles following single intravenous injection in rats: implications for magnetic resonance imaging. *Cell Tissue Res*. 2004;316:315-323.
45. Jordan A, Scholz R, Wust P, Fähling H, Felix R. Magnetic fluid hyperthermia (MFH): Cancer treatment with AC magnetic field induced excitation of biocompatible superparamagnetic nanoparticles. *Journal of Magnetism and Magnetic Materials*. 1999;201:413-419.
46. Johannsen M, Gneveckow U, Thiesen B, et al. Thermotherapy of prostate cancer using magnetic nanoparticles: feasibility, imaging, and three-dimensional temperature distribution. *Eur Urol*. 2007;52:1653-1661.
47. Gonzales M, Krishnan KM. Synthesis of magnetoliposomes with monodisperse iron oxide nanocrystal cores for hyperthermia. *Journal of Magnetism and Magnetic Materials*. 2005;293:265-270.
48. Vander Vorst A, Rosen A, Kotsuka Y. RF/Microwave interaction with biological tissues. Vol 181: John Wiley & Sons; 2006.
49. Coley WB. The Treatment of Inoperable Sarcoma by Bacterial Toxins (the Mixed Toxins of the Streptococcus erysipelas and the Bacillus prodigiosus). *Proc R Soc Med*. 1910;3:1-48.
50. Gas P. Essential Facts on the History of Hyperthermia and their Connections with Electromedicine. *Electrical Review*. 2011;87:37-40.
51. Westermarck N. The Effect of Heat upon Rat-Tumors¹. *Skandinavisches Archiv Für Physiologie*. 1927;52:257-322.
52. Dewey WC, Hopwood LE, Sapareto SA, Gerweck LE. Cellular responses to combinations of hyperthermia and radiation. *Radiology*. 1977;123:463-474.
53. Johnson HA, Pavelec M. Thermal enhancement of thio-TEPA cytotoxicity. *Journal of the National Cancer Institute*. 1973;50:903-908.
54. Gilchrist RK, Medal R, Shorey WD, Hanselman RC, Parrott JC, Taylor CB. Selective inductive heating of lymph nodes. *Ann Surg*. 1957;146:596-606.

55. Ortega D. Magnetic hyperthermia. in: Pankhurst QA, ed. Nanostructures through Chemistry. Vol 1. Nanoscience: Royal Society of Chemistry, Cambridge; 2013:60-88.
56. Atkinson WJ, Brezovich IA, Chakraborty DP. Usable frequencies in hyperthermia with thermal seeds. *IEEE Trans Biomed Eng.* 1984;31:70-75.
57. Brezovich IA, Meredith RF. Practical aspects of ferromagnetic thermoseed hyperthermia. *Radiol Clin North Am.* 1989;27:589-602.
58. Jain TK, Reddy MK, Morales MA, Leslie-Pelecky DL, Labhasetwar V. Biodistribution, clearance, and biocompatibility of iron oxide magnetic nanoparticles in rats. *Mol Pharm.* 2008;5:316-327.
59. Endrich B, Hammersen F, Messmer K. Hyperthermia-induced changes in tumor microcirculation. *Recent Results Cancer Res.* 1988;107:44-59.
60. Heldin CH, Rubin K, Pietras K, Ostman A. High interstitial fluid pressure - an obstacle in cancer therapy. *Nat Rev Cancer.* 2004;4:806-813.
61. Johannsen M, Thiesen B, Jordan A, et al. Magnetic fluid hyperthermia (MFH) reduces prostate cancer growth in the orthotopic Dunning R3327 rat model. *Prostate.* 2005;64:283-292.
62. Yanase M, Shinkai M, Honda H, Wakabayashi T, Yoshida J, Kobayashi T. Intracellular hyperthermia for cancer using magnetite cationic liposomes: an in vivo study. *Cancer Science.* 1998;89:463-470.
63. Rabias I, Tsitrouli D, Karakosta E, et al. Rapid magnetic heating treatment by highly charged maghemite nanoparticles on Wistar rats exocranial glioma tumors at microliter volume. *Biomicrofluidics.* 2010;4:024111.
64. Otsuka T, Yonezawa M, Kamiyama F, Matsushita Y, Matsui N. Results of surgery and radio-hyperthermo-chemotherapy for patients with soft-tissue sarcoma. *Int J Clin Oncol.* 2001;6:253-258.
65. Pennacchioli E, Fiore M, Gronchi A. Hyperthermia as an adjunctive treatment for soft-tissue sarcoma. *Expert Rev Anticancer Ther.* 2009;9:199-210.
66. Wust P, Hildebrandt B, Sreenivasa G, et al. Hyperthermia in combined treatment of cancer. *Lancet Oncol.* 2002;3:487-497.
67. Moroz P, Jones SK, Winter J, Gray BN. Targeting liver tumors with hyperthermia: ferromagnetic embolization in a rabbit liver tumor model. *Journal of surgical oncology.* 2001;78:22-29.
68. Lee JH, Jang JT, Choi JS, et al. Exchange-coupled magnetic nanoparticles for efficient heat induction. *Nat Nanotechnol.* 2011;6:418-422.

69. Matsumine A, Takegami K, Asanuma K, et al. A novel hyperthermia treatment for bone metastases using magnetic materials. *Int J Clin Oncol*. 2011;16:101-108.
70. Hilger I, Frühauf K, Andrä W, Hiergeist R, Hergt R, Kaiser WA. Heating potential of iron oxides for therapeutic purposes in interventional radiology. *Acad Radiol*. 2002;9:198-202.
71. Mahjoob S, Vafai K. Analytical characterization of heat transport through biological media incorporating hyperthermia treatment. *International Journal of Heat and Mass Transfer*. 2009;52:1608-1618.
72. Andrä W, d'Ambly CG, Hergt R, Hilger I, Kaiser WA. Temperature distribution as function of time around a small spherical heat source of local magnetic hyperthermia. *Journal of Magnetism and Magnetic Materials*. 1999;194:197-203.
73. Vaupel P. Tumor microenvironmental physiology and its implications for radiation oncology. *Seminars in radiation oncology*. Vol 14: Elsevier; 2004:198-206.
74. Less JR, Skalak TC, Sevick EM, Jain RK. Microvascular network architecture in a mammary carcinoma. *EXS*. 1992;61:74-80.
75. Kim D, Park K. Swelling and mechanical properties of superporous hydrogels of poly (acrylamide-co-acrylic acid)/polyethylenimine interpenetrating polymer networks. *Polymer*. 2004;45:189-196.
76. Spells KE. The Thermal Conductivities of some Biological Fluids. *Physics in Medicine and Biology*. 1960;5:139.

BIOGRAPHICAL SKETCH

Born in Goa, India in 1989, Jolin Rodrigues has always been passionate about her Indian heritage, even though she spent her growing years in the tiny but powerful nation of Qatar in the Middle East. Having finished high school in Qatar, she moved back to her beloved India to pursue an undergraduate Engineering degree in Biotechnology at the People's Education Society Institute of Technology, one of the premier engineering colleges in the country. Her love of teaching led her to become a Teaching Assistant during her junior year of her college, and was also actively involved in the events hosted by the Biotechnology Department. During her undergraduate years, her enthusiasm propelled her to become one of the organizers of the annual techno-cultural fest of her college, besides being on the editorial board of the college magazine.

While at college, she attended various biotechnology conferences and realized a newfound love for biomaterials and tissue engineering. Her pursuit of these fields brought her to the University of Florida, miles away from the comfort of her loving family and childhood friends. But the two years spent in Gainesville has taught her more than what she hoped to gain, with valuable experiences gaining her a new perspective on life, and great friends who have helped her in more ways than one. She hopes to join the bioscience industry and become a successful bio-entrepreneur someday. Besides poring endlessly over scientific papers, Jolin finds great thrill in outdoor adventures, reading novels, travelling and experiencing new culinary delights.